

AD

AD-E402 821

Technical Report ARWEC-TR-97010

## ANALYSIS OF THE PENETRATION RESISTANCE OF CONCRETE

Vladimir M. Gold

August 1997

DTIC QUALITY INSPECTED 2



US ARMY  
TANK AUTOMOTIVE AND  
ARMAMENTS COMMAND  
ARMAMENT RDE CENTER

### U.S. ARMY ARMAMENT RESEARCH, DEVELOPMENT AND ENGINEERING CENTER

Warheads, Energetics & Combat-support Armaments Center

Picatinny Arsenal, New Jersey

Approved for public release; distribution is unlimited.

19970916 150

The views, opinions, and/or findings contained in this report are those of the authors(s) and should not be construed as an official Department of the Army position, policy, or decision, unless so designated by other documentation.

The citation in this report of the names of commercial firms or commercially available products or services does not constitute official endorsement by or approval of the U.S. Government.

Destroy this report when no longer needed by any method that will prevent disclosure of its contents or reconstruction of the document. Do not return to the originator.

**REPORT DOCUMENTATION PAGE**Form Approved  
OMB No. 0704-0188

Public reporting burden for this collection of information is estimated to average 1 hour per response, including the time for reviewing instructions, searching existing data sources, gathering and maintaining the data needed, and completing and reviewing the collection of information. Send comments regarding this burden estimate or any other aspect of this collection of information, including suggestions for reducing this burden to Washington Headquarters Services, Directorate for Information Operations and Reports, 1215 Jefferson Davis Highway, Suite 1204, Arlington, VA 2202-4302, and to the Office of Management and Budget, Paperwork Reduction Project (0704-0188), Washington, DC 20503.

1. AGENCY USE ONLY (Leave Blank)		2. REPORT DATE August 1997	3. REPORT TYPE AND DATES COVERED Final
4. TITLE AND SUBTITLE ANALYSIS OF THE PENETRATION RESISTANCE OF CONCRETE			5. FUNDING NUMBERS A3 PE 6226 18
6. AUTHOR(S) Vladimir M. Gold			
7. PERFORMING ORGANIZATION NAME(S) AND ADDRESS(ES) ARDEC, WECAC Energetics and Warhead Division (AMSTA-AR-WEE-C) Picatinny Arsenal, NJ 07806-5000			8. PERFORMING ORGANIZATION REPORT NUMBER
9. SPONSORING/MONITORING AGENCY NAME(S) AND ADDRESS(ES) ARDEC, WECAC Information Research Center (AMSTA-AR-WEL-TL) Picatinny Arsenal, NJ 07806-5000			10. SPONSORING/MONITORING AGENCY REPORT NUMBER  Technical Report ARWEC-TR-97010
11. SUPPLEMENTARY NOTES			
12a. DISTRIBUTION/AVAILABILITY STATEMENT  Approved for public release; distribution is unlimited.			12b. DISTRIBUTION CODE
13. ABSTRACT A combined numerical and analytical study of penetration of concrete by high velocity (~1.8 km/s) projectiles was conducted. The effects of concrete's constitutive modeling on penetration calculations were studied and are discussed. The results of the analysis are compared with the available experimental data. All constitutive models studied accounted for the compressibility of concrete. The plastic yield condition was modeled with the von Mises yielding criterion using: (1) constant yield-strength model and (2) pressure-dependent yield-strength model. Regardless of the value of the yield strength, application of a constant yield strength model resulted in nearly identical hole profiles which, in all cases, significantly disagreed with the experimental data. Crater profiles calculated with the pressure-dependent yield model showed good agreement with the available experimental data. The reduction in the calculated crater profiles was attributed to the increased target resistance to penetration. A detailed analysis of the flow field along the central streamline shows that increases in the target's resistance to penetration are due to the growth in the time rate of the projectile erosion.			
14. SUBJECT TERMS Theory of penetration      Concrete target      Projectile  Target resistance      Plastic zone			15. NUMBER OF PAGES  41
			16. PRICE CODE
17. SECURITY CLASSIFICATION OF REPORT  UNCLASSIFIED	18. SECURITY CLASSIFICATION OF THIS PAGE  UNCLASSIFIED	19. SECURITY CLASSIFICATION OF ABSTRACT  UNCLASSIFIED	20. LIMITATION OF ABSTRACT  SAR

## NOTATIONS

The following symbols are used in this paper:

$A_i$ and $B_j$	empirical coefficients $i=0,\dots,3, j=0,\dots,2$
$E$	internal energy
$I$	second invariants of the strain rate tensor
$J_2$	second invariant of the deviatoric stress tensor
$k, k(p)$	Von Mises yield strength, pressure-dependent yield strength
$l$	instantaneous penetrator length
$p, p_c$ , and $p_s$	pressure, compaction pressure, and pressure of the solid phase
$p_0, p_1$	coefficients
$\bar{p}, \dot{p}(t)$	time average pressure
$R_h$ and $R_s$	hydrodynamic and shear stress components of the pressure at the target/penetrator interface, respectively
$R_t$	empirical target strength factor
$r$	radial coordinate
$s_{ij}$	deviatoric stress tensor, $i,j=r,z,\theta$
$T, t$	time
$V_0$	initial projectile velocity
$v$	velocity of the rigid portion of the penetrator
$v_r$ and $v_z$	radial and axial component of the velocity
$u$	penetration rate
$Y, Y(p)$	yield strength
$Y_p$	empirical penetrator strength factor
$z$	axial coordinate

$z_0$ and $z_{ep}$	axial position of the target/penetrator interface and the elastic-plastic boundary, respectively
$\gamma$	equivalent plastic strain
$\dot{\epsilon}_{ij}, \dot{\gamma}_{ij}$	components of the strain rate tensor $i,j=r,z,\theta$
$\epsilon_{1p}, \epsilon_{2p},$ and $\epsilon_{3p}$	principle plastic strain components
$\Delta$	size of the plastic zone in front of the penetrator
$\Delta p$	pressure gradient in the plastic zone in front of the penetrator
$\Delta s_{zz}$	stress deviatoric component of the pressure at the target/penetrator interface
$\theta$	angular coordinate
$\rho, \rho_r,$ and $\rho_s$	density, reference density, and density of the solid phase, respectively
$\rho_t, \rho_{t0}, \rho_t(z)$	target density
$\sigma_{ij}$	stress tensor, $i,j=r,z,\theta$
$\sigma_n$	normal stress at a boundary
$\phi, \phi_0$	porosity, initial porosity

## CONTENTS

	Page
Introduction	1
Concrete Penetration Experiments and the Numerical Model	2
Results of the Numerical Analysis	7
Analysis of the Axial Momentum Balance Equation on the Line of Axial Symmetry	10
The Effect of the Target Constitutive Modeling	15
Conclusions	19
References	33
Distribution List	35

## FIGURES

	Page
1. Initial configuration of the computational domain: spherical-nose copper projectile impacting a right circular cylinder of concrete with velocity $V_0=0.1836 \text{ cm}/\mu\text{s}$	21
2. Resulting hole profiles employing (a) the constant yield-strength model and (b) the pressure dependent yield-strength model	22
3. History of pressure $p=p(t)$ at the target/penetrator interface at $r=0$ for various constitutive models	23
4. Empirical yield strength function $Y=Y(p)$ for the pressure dependent yield-strength model	24
5. Structure of the elastic-plastic flow field in target (time $t=35 \mu\text{s}$ , $\gamma=0.062$ )	25
6. Calculated profiles of (a) $s_{zz}$ and (b) $s_{rz,r}$ along the center line $r=0$ for the constant yield-strength and the pressure dependent yield-strength models ( $t=35 \mu\text{s}$ )	26
7. Comparison between the instantaneous values of various terms comprising the pressure at the target/penetrator interface ( $t=35 \mu\text{s}$ )	28
8. Trajectories of the front and the rear of the penetrator for the constant yield-strength and the pressure dependent yield-strength models	29
9. Calculated profiles of the axial component of velocity $v_z$ at the center line $r=0$ ( $t=35 \mu\text{s}$ )	30
10. Calculated profiles of pressure $p$ along the center line $r=0$ ( $t=35 \mu\text{s}$ )	31
11. Profiles of the radial velocity component $v_r$ versus radial coordinate $r$ ( $z=5.2 \text{ cm}$ , $t=35 \mu\text{s}$ )	32

## INTRODUCTION

When a high-velocity projectile impacts and penetrates a semi-infinite body of concrete, the penetration is accomplished by displacing the target material radially and as a result a tunnel-shaped crater is formed in the target. The target resistance to penetration (which is inferred by the depth and diameter of the produced hole) depends on a number of parameters including the projectile velocity and the relative strength of the projectile and the target. In particular, when the penetrator velocity is fixed, the structure of the plastic flow field in the target defines the extent of the ensuing target material displacements (both the radial and the axial) which in turn determines the size of the resulting crater. Therefore, since the structure of this flow field is controlled primarily by the yield-strength properties of the target, the constitutive behavior of the target material is the principle factor that determines the target's resistance to penetration.

Under the pressures exerted at the interface between the projectile and the target, the penetrator nose may deform into a characteristic mushroom-like shape. The extent of this deformation varies significantly with the impact velocity and the relative strength of the projectile and the target. For impact velocities exceeding 1.2 to 1.5 km/s, the strength of most penetrator materials is not sufficient to prevent penetrator deformation and mushrooming, resulting in significant penetrator erosion. Recent experimental work by Gold et al. (ref 1) showed that for velocities exceeding 1.5 km/s the penetrator erodes almost entirely, implying that penetration of a semi-infinite body of concrete can be successfully predicted employing the one-dimensional modified (i.e., strength dependent) hydrodynamic theory of penetration (ref 2). Within the framework of this theory, the essence of the mechanics of penetration of a solid projectile into a solid target is represented through erosion of the penetrator material in combination with its rigid body motion. According to the theory, the strength properties of the penetrator and the target are represented with two empirical strength factors  $Y_p$  and  $R_t$ , usually referred to as the penetrator and target "strengths," respectively. For each combination of the penetrator and target materials, the empirical strength factors  $Y_p$  and  $R_t$  have to be determined experimentally. One of the principle conclusions of the modified hydrodynamic theory of penetration is that the target resistance to penetration is proportional to the target strength factor  $R_t$ , a fact supported by a vast amount of experimental data.

The analytical structure of the parameter  $R_t$  has been examined by a number of researches including Tate (refs 3 and 4), Pidsley (ref 5), and Anderson and Walker (refs 6 and 7) both analytically and numerically. Because the assumptions of the modified hydrodynamic theory of penetration neglect the complexity of the structure of the target elastic-plastic flow field, the discrepancy between the experimental values of  $R_t$  and the numerical predictions is rather significant. For example, in contradiction to the assumptions of the modified hydrodynamic theory, the numerical results of Anderson and Walker (refs 6 and 7) showed that during the penetration the magnitude of  $R_t Y_p$  is not constant, but changes as the penetrator penetrates the target. The analysis presented in this work examines the relationship between the target strength factor  $R_t$  and the target resistance to penetration.



Concrete is a complex material consisting of mineral aggregate bound by cement paste containing a large amount of water and voids. In the present work, two concrete yield-strength models were studied: (1) the constant yield-strength model and (2) the pressure-dependent yield-strength model. In the case of the constant yield model, the disagreement between the calculated hole profiles and the experimental data was rather significant, regardless of the value of the yield strength parameter  $k$ . In the case of the pressure-dependent yield-strength model, the analysis resulted in hole predictions which not only reproduced the experimental depth of penetration but also matched the measurements of the profile of the tunnel portion of the crater.

The reduction in the calculated penetration channel diameters (with the introduction of the pressure-dependent yield strength) was attributed to the increased target resistance to penetration. In order to clarify the effect of the constitutive modeling on the penetration calculations, further analysis concentrated on studying the parameters of the flow field along the central streamline. Along the centerline a number of flow field parameters vanish, thus permitting significant simplification of the momentum balance equation. Assuming that the penetration is steady state, the momentum balance equation can be integrated resulting in an explicit expression for the pressure at the target/penetrator interface. In this expression, the target resistance to penetration is represented by the following terms: (1) the difference between stress deviators at the elastic-plastic boundary and the target/penetrator interface, respectively, (2) the pressure at the elastic-plastic boundary, and (3) the integral of the radial gradient of the shear stress deviator (at the central streamline) evaluated within the limits of the plastic zone. A detailed analysis of the above terms shows that inclusion of the yield strength-pressure dependency in the constitutive model significantly increases the target resistance to penetration. As a result, the time rate of projectile erosion increases, which ultimately leads to significant reduction in the calculated penetration depths and hole diameters.

## **CONCRETE PENETRATION EXPERIMENTS AND THE NUMERICAL MODEL**

The experiments and numerical modeling referred to in the present study have been reported extensively in the literature (refs 1 and 8) and will be briefly presented here for completion. Copper and tantalum projectiles were launched by gun against semi-infinite concrete and reinforced concrete targets with velocities ranging from 0.15 cm/ $\mu$ s to 0.19 cm/ $\mu$ s. The projectiles were spherical-nose, right circular cylinders with diameters of 1.3 cm and 2.0 cm, and length-to-diameter ratios varying from 3.9 to 14.6. The projectile's launching velocities were measured from streak camera records. Orthogonal flash x-rays in the immediate vicinity of the surface of the target independently verified the impact velocities and provided information on the yaw and condition of projectiles just prior to the impact.

The targets were right circular cylinders 91 cm in diameter and 91 cm long and were constructed from concrete with maximum aggregate size of 1.9 cm and density of 2.24 g/cm<sup>3</sup>. Laboratory testing of specimens of this concrete resulted in an average unconfined compressive strength of approximately 0.374 Kbar. The targets were instrumented with a sequence of break gages that were carefully positioned with reference to the front surface and spaced 2.54 cm apart from each other. The gages were 0.03-cm thick printed circuit boards consisting of two conductive copper foils and enclosing an insulated copper foil maze between them. Although it is rather difficult to define the exact mode of gage failure, it is reasonable to assume that once the strain exceeds that of the elastic limit of the weakest material (insulation), the gage "breaks." When the projectile penetration rate is below the sonic velocity of the target material, concrete that is crushed in front of the projectiles forms a well defined plastic zone of a finite size. Therefore, assuming that the "strengths" of the gage and the concrete are approximately the same, the gage would "break" approximately at the time when the elastic-plastic boundary arrives at the position of the gage. Thus, the succession of trigger times of the break gages determines the trajectory of the elastic-plastic boundary in front of the projectile.

In all experiments the resulting crater profiles were carefully measured. In the case of the 1.3-cm diameter projectiles, crater entrances were approximately 25 cm in diameter; the penetration channel rapidly narrowed down to a diameter of 5 cm, 10.5 cm away from the surface of the target. The deeper portion of the crater had a characteristic form of a well rounded and slightly tapered tunnel. Measurements of this portion of the crater were used for validating the accuracy of different constitutive models for concrete studied in this work.

In the present work, the numerical experiments concentrated on modeling a representative experiment with a 19-cm long and 1.3-cm diameter copper projectile impacting a plain concrete target with velocity  $V_0 = 0.1836$  cm/ $\mu$ s [test PA8Cu1.4 (ref 1)]. The numerical analysis presented here was performed using the CALE (ref 9) computer program. CALE is a plane two-dimensional and three-dimensional axisymmetric hydrodynamics code based on an Arbitrary Lagrangian Eulerian formulation of the governing equations. It can run in a pure Lagrangian mode, a pure Eulerian mode, or in an arbitrary hybrid mode. In the Eulerian reference frame the description of the axisymmetric kinematic deformation of the continuum is given by the following conservation laws:

### **Conservation of mass**

$$\frac{\partial \rho}{\partial t} + v_r \frac{\partial \rho}{\partial r} + v_z \frac{\partial \rho}{\partial z} + \rho \left( \frac{1}{r} \frac{\partial (r v_r)}{\partial r} + \frac{\partial v_z}{\partial z} \right) = 0 \quad (1)$$

### **Conservation of linear momentum**

$$\frac{\partial v_r}{\partial t} + v_r \frac{\partial v_r}{\partial r} + v_z \frac{\partial v_r}{\partial z} = (1/\rho) \cdot (\frac{\partial \sigma_{rr}}{\partial r} + \frac{\partial (\sigma_{rz} + p)}{\partial z} + (\sigma_{rr} + \sigma_{zz} + 2 \cdot p)/r) \quad (2a)$$

$$\frac{\partial v_z}{\partial t} + v_r \frac{\partial v_z}{\partial r} + v_z \frac{\partial v_z}{\partial z} = (1/\rho) \cdot (\frac{\partial \sigma_{zz}}{\partial z} + \frac{\partial (\sigma_{rz} + p)}{\partial r} + (\sigma_{rz} + p)/r) \quad (2b)$$

## Conservation of energy

$$\begin{aligned} \partial E / \partial t + v_r \cdot \partial E / \partial r + v_z \cdot \partial E / \partial z = (1/\rho) \cdot [-p \cdot ((1/r) \cdot \partial(r \cdot v_r) / \partial r + \partial v_z / \partial z) + r \cdot (\partial(v_r/r) / \partial r) \cdot (\sigma_{rr} + p) \\ + (\sigma_{zz} + p) \cdot (\partial v_z / \partial z - v_r/r) + (\sigma_{rz} + p) \cdot (\partial v_r / \partial z - \partial v_z / \partial r)] \end{aligned} \quad (3)$$

Body forces (such as gravity) and heat conduction are ignored.

CALE's procedure for calculating elastic-plastic flow is based on the methodology developed by Wilkins (refs 10 and 11). The stress behavior of a material can be thought of being composed of a stress associated with uniform hydrostatic pressure  $p$ , referred to as the spherical part of the stress tensor, plus the stress associated with the resistance of the material to shear distortion, referred to as the deviator  $s_{ij}$ . In describing yielding and plastic flow, the stress contributions that are due to shear distortion are limited by the constitutive equation for the material. The stress tensor is given then by

$$\sigma_{ij} = -p + s_{ij} \quad (4)$$

The constitutive equation for the projectile material adopted here is that of Steinberg-Guinan (ref 12), which specifies the shear modulus and the yield strength as a function of pressure, temperature, and equivalent plastic strain. The equation of state (EOS) that was used to model the hydrodynamic response of copper was the standard linear polynomial approximation usually employed for metals and adopted by Tipton (ref 9) for the CALE code. Since the copper projectiles were manufactured from a standard stock of oxygen-free high conductivity (OFHC) copper, the analysis relied on a standard set of parameters for this material given by Tipton (ref 13). Details of these models and their implementation can be found in Tipton (ref 9).

In modeling the constitutive response of concrete targets, all models studied accounted for compressibility of concrete. The nonlinearity in the Hugoniot data for the concrete for particle velocities below 1 km/s has been attributed to the effects of microcracking and pore closure, and was modeled with a porous material equation of state. Using a porous EOS model, Read and Maiden (ref 14) were able to reproduce the essential features of the experimental shock-velocity versus particle-(material)-velocity data. The particle velocities experienced by the concrete in the earlier penetration experiments of Gold *et al.* (ref 1) are in the very same range. Therefore, employment of the porous EOS model is ideally suited to the conditions of high velocity penetration.

Following Tipton (ref 15), the porous EOS model assumes that, while in compression, the porosity is not changed until the pressure exceeds the compaction pressure,  $p_c$ . In tension, the porosity is not increased until the pressure drops below  $-p_c$ . The compaction pressure is assumed to be a function of the porosity  $\phi$  and has the following form

$$p_c = -p_0 \cdot \log(\phi) \quad (5)$$

The total pressure of the porous material is given by

$$p = (1-\phi) \cdot p_s(\rho_s) \quad (6)$$

where  $\phi$  is the porosity and  $p_s$  and  $\rho_s$  are the pressure and the density of the solid phase, respectively. The EOS for the solid phase is taken in a polynomial form

$$p_s = A_0 + A_1\mu + A_2\mu^2 + A_3\mu^3 + (B_0 + B_1\mu + B_2\mu^2)E \quad (7)$$

where  $E$  is the internal energy,  $\mu = \rho/\rho_r - 1$ ,  $\rho_r = \rho_0/(1-\phi_0)$  is the reference density, and  $\phi_0$  is the initial porosity. Further details on this model and its implementation in CALE can be found in Tipton (ref 1).

CALE's procedure for calculation of the elastic-plastic flow employs the von Mises yielding criterion. The yielding behavior of concrete was modeled using the following constitutive equations:

#### (1) Constant yield-strength model

$$J_2 = k^2 = \text{Const} \quad (8)$$

#### (2) Pressure dependent yield-strength model

$$J_2 = k^2(p) \quad (9)$$

In these models,  $J_2$  is the second deviatoric stress invariant given by

$$J_2 = \frac{1}{2} \cdot (s_{rr}^2 + s_{\phi\phi}^2 + s_{zz}^2) + s_{r\phi}^2 + s_{rz}^2 + s_{z\phi}^2 \quad (10)$$

and  $k$  or  $k(p)$  are either an empirical strength constant or an empirical function (of pressure  $p$ ), respectively. The relationship between the experimental strength data and  $k$  is as follows: consider an ideal test in which a specimen is subject to a simple tension/compression in the  $z$ -direction (i.e.  $\sigma_{zz} = Y$ ), while the rest of the stress components vanish  $\sigma_{ij} = 0$ . In the case of a constant strength model given by equation 8,  $J_2 = Y^2/3$ , or  $k = Y/\sqrt{3}$ . In the case of the pressure dependent yield model, the empirical strength function  $k(p)$  is obtained directly from triaxial compression test data (ref 16).

The geometry and boundary conditions are shown in figure 1. The domain considered is axisymmetric in  $r$ - $z$  space. Domain  $T_1T_2T_3T_4$  represents the target,  $P_1P_2P_3T_1$  is the spherical-nose projectile, and the rest of the domain  $E_1E_2T_2T_1$  is filled with air. Eight 0.03-cm thick break gages were initially modeled using three computational cells, each 0.01-cm thick, filled with copper. After some initial numerical experimentation it became clear that

these 0.01 cm cells were resulting in very small time steps, which controlled the overall speed of the calculations. Therefore, in order to decrease the otherwise prohibitively excessive computational time, the number of cells across the thickness of the break gages was reduced to one. A more detailed description of the computational mesh employed in the model can be found in Gold *et al.* (ref 8).

The initial and the boundary conditions are as follows:

$$\begin{aligned} \text{at } t=0 \quad v_r=0, v_z=V_0 \quad & \text{in domain } P_1P_2P_3T_1 \\ v_r=v_z=0 \quad & \text{everywhere inside of } E_1E_2T_3T_4, \text{ except } P_1P_2P_3T_1 \end{aligned} \quad (11)$$

$$\begin{aligned} \text{at } t \geq 0 \quad v_r=v_z=0 \quad & \text{along } E_1E_2 \\ \sigma_n=0 \quad & \text{along } E_2T_3 \text{ and } T_3T_4 \\ v_r=0 \quad & \text{along } E_1T_4 \text{ (line of axial symmetry)} \end{aligned} \quad (12)$$

## RESULTS OF THE NUMERICAL ANALYSIS

The analysis presented in this work addresses a number of issues pertaining to constitutive modeling of concrete in high velocity penetration analysis. Two concrete yield-strength models were studied: (1) the constant yield-strength model given by equation 8, and (2) the pressure dependent yield-strength model, given by equation 9. Hole profiles resulting from the numerical experimentation with these models are shown in figure 2a and b. In the case of the constant yield model, the disagreement between the calculated hole profiles and the experimental data was rather significant (fig. 2a), regardless of the value of the yield strength parameter  $k$  [the von Mises yield strength  $k=Y/\sqrt{3}$  was varied in the relatively wide range from  $Y=0.187$  Kbar to  $Y=1.8$  Kbar, while the unconfined compressive strength of the concrete was approximately 0.374 Kbar (ref 1)]. Since the numerical experiments resulted in almost identical penetration channel diameters (which all significantly disagreed with the experimental data), it follows then that the poor predictive capability of the constant yield-strength model cannot be improved by mere "adjustment" of the strength parameter  $k$ .

In the case of the pressure-dependent yield-strength model (eq. 9) the analysis resulted in hole predictions, which not only reproduced the experimental depth of penetration, but also matched the measurements of the profile of the tunnel portion of the crater (fig. 2b). It follows then that mere inclusion of the yield-strength-pressure dependency in the concrete constitutive model results in a rather significant decrease in the hole profile

predictions, apparently due to the increased target resistance to penetration. Thus, before one even attempts to understand the relationship between the target constitutive modeling and the target resistance to penetration, one has to identify principle factors which determine the capability of a target material to resist penetration.

It can be hypothesized that one of the principle parameters that affect target resistance to penetration is the pressure at the target/penetrator interface. The calculated histories of pressure at the target/penetrator interface (at the centerline  $r=0$ ) are shown in figure 3. According to numerous experimental and analytical studies, the penetration process can be differentiated into the following three stages (e.g, refs 17 and 18): (1) the initial transient stage, (2) the quasi steady-state penetration, and (3) penetrator deceleration. As seen from figure 3, during the initial transient stage (which lasts up to approximately 40  $\mu$ s) and during the steady-state penetration (that continues to approximately 280  $\mu$ s), all the calculated pressure histories are almost identical. It is only in the final stage of the penetration, when the projectile debris start to decelerate rapidly (which occurs after approximately 280  $\mu$ s), that the pressure history curves become distinguishable from each other. As seen from figure 3, these later portions of the curves are distinguishable from each other only because of the difference in their respective starting times (which correlate well with hypothetical changes in target "strengths"). After "branching off", all curves are approximately parallel. This indicates that changes in the constitutive model affect only the commencement of the last stage of the penetration, while the rates of the deceleration stay approximately the same. Therefore, if there exist a difference in the penetration characteristics, this difference must manifest itself during the stage of the steady-state penetration.

During the quasi steady-state penetration, the motion of the penetrator can be viewed within the framework of the one-dimensional modified hydrodynamic theory of penetration (refs 2, 3, and 19). According to this theory, pressure at the target/penetrator interface is given by the following

$$\frac{1}{2} \cdot \rho_{p0}(v-u)^2 + Y_p = \frac{1}{2} \cdot \rho_{t0}u^2 + R_t \quad (13)$$

where  $\rho_{p0}$  and  $\rho_{t0}$  are densities of the penetrator and the target, respectively. The velocity of the undeformed portion of the penetrator is  $v$ ,  $u$  is the penetration rate, and  $Y_p$  and  $R_t$  are empirical parameters relating to strengths of penetrator and target materials, respectively.

In this simplistic one-dimensional model, the pressure at the target/penetrator interface is determined only as a function of local flow field variables such as the velocity, the physical properties, etc. However, in the case of the three-dimensional analysis, the pressure is also influenced by the presence of the free boundary, which reflects the traveling stress waves back into the target domain. Inside the target domain the pressure wavelets interfere and superimpose, resulting in large fluctuations of the flow field parameters that are sensitive to the continuum stress wave propagation properties. Therefore, in order to



compare these typically erratic and rapidly changing parameters, one has to redefine them on a time average basis. Adopting an approach suggested by Anderson and Walker (ref 6), the time averaged pressure can be defined as follows:

$$\bar{p} = \frac{1}{T} \cdot \int_0^T p \cdot dt \quad (14)$$

where  $t$  is the time,  $p=p(t)$  is the pressure at the target/penetrator interface, and  $T$  is the duration of the quasi steady-state stage. However, even during this quasi steady-state stage of penetration, the penetrator slightly decelerates, and, therefore, the pressure at the target/penetrator interface changes with time. Since equation 14 completely ignores these effects, the notion of the time averaged pressure can be modified assuming a linear dependency between the average pressure  $\bar{p}$  and the time

$$\bar{p}(t) = p_0 + p_1 t \quad (15)$$

Coefficients  $p_0$  and  $p_1$  can be easily determined by minimizing the following expression

$$\chi^2(p_0, p_1) = \sum_i^N \left[ \frac{p_i - p_0 - p_1 t_i}{\sigma_i} \right]^2 \quad (16)$$

where  $p_i$  are the values of pressure at given times  $t_i$ ,  $i=1, \dots, N$ , and  $\sigma_i$  is the standard deviation. Employing this notion of the time averaged pressure, one can readily examine the effect of the target constitutive modeling on the pressure at the target/penetrator interface. The histories of the time averaged pressure  $\bar{p}$  at the target/penetrator interface are given in the enlarged segment of figure 3. These results show that, in agreement with the hydrodynamic theory of penetration, the target/penetrator interface pressure increases with increases in the "target strength," a tendency that may be intuitively associated with the effect of the von Mises yield strength  $k$  or  $k(p)$ .

The empirical yield strength function (ref 16)  $Y=Y(p)$ , which was employed in the analysis using the pressure-dependent yield model, is shown in figure 4. During the quasi steady-state penetration the average pressure at the target/penetrator interface is approximately 0.02 Mbar. Therefore, according to figure 4, the corresponding averaged yield strength at the projectile/target interface is approximately 1.6 Kbar. Intuitively, one would expect that the higher values of the "average" strength have to result in the higher values of the pressures. And yet, the calculations show (see  $\bar{p}$  in fig. 3) that in the case of the pressure-dependent yield model (the "average" yield is approximately 1.6 Kbar), the time-averaged pressure  $\bar{p}$  is higher than the pressure resulting from the 1.8 Kbar constant yield model. It follows then, that the target resistance to penetration is not related simply either to the pressure or to the yield strength alone. In order to identify the principle factors affecting the target resistance to penetration, one has to examine the structure of the plastic flow field in the target.

The structure of the elastic-plastic flow field in the target can be examined from the results presented in figure 5. Isolines of the equivalent plastic strain shown in figure 5, represent the approximate position of the elastic-plastic boundary in the target. The equivalent plastic strain is defined as

$$\gamma = \frac{2}{3} \cdot \sqrt{(\epsilon_{1P} - \epsilon_{2P})^2 + (\epsilon_{2P} - \epsilon_{3P})^2 + (\epsilon_{3P} - \epsilon_{1P})^2} \quad (17)$$

where  $\epsilon_{1P}$ ,  $\epsilon_{2P}$ , and  $\epsilon_{3P}$  are the principal plastic strain components. The equivalent plastic strain is one of the principal parameters of the plastic flow field which reflects the extent of plastic state, and the isolines of  $\gamma$  characterize the structure of the deformation field. In the elastic region the plastic strain components vanish, and  $\gamma=0$ . In the plastic region  $\gamma>0$ , whereas the isolines of a small  $\gamma$  mark the approximate position of the elastic-plastic boundary.

Employing numerical experimentation, one may attempt to construct a reasonable approximation to the plastic flow around the penetrator, an approach useful in a number of the approximate theories of high velocity penetration. It is interesting to note that all numerical experiments resulted in isolines with shapes that are approximately hemispherical, regardless of the employed target constitutive model. The hemispherical symmetry in the target deformation field appears to be an intrinsic characteristic of the high velocity penetration process proper, rather than a result of a particular type of a constitutive model. This observation is also supported by the results of high velocity penetration analysis for various metallic targets (e.g., refs 5 and 20 through 23).

Since the target deformation field is hemispherically symmetric, the center line  $r=0$  seems to be the most attractive choice for referencing both the motion of the penetrator in the target and the flow of the target material around the penetrator. Referring to figure 5,  $z_0$  denotes the position of the interface between the penetrator and the target, while the coordinate of the elastic-plastic boundary is given by  $z_{ep}$ . Thus, the plastic zone in front of the penetrator is described by a single parameter  $\Delta=z_{ep}-z_0$ . The interrelationship between  $\Delta$  and the target resistance to penetration is as follows.

Consider a balance of energy for the plastic zone  $z_{ep}(t) \geq z \geq z_0(t)$  enclosed within an idealized control volume, which moves through the target with a velocity equal to the penetration rate  $u$ . In the frame of reference which moves with velocity  $u$ , the energy (in the form of plastic work) is influxed into the control volume through the boundary  $z_0$ . The amount of this energy  $E_0$  is determined by the penetrator erosion rate  $v-u$ , and ultimately, by the kinetic energy of the penetrator. The efflux of energy out of the control volume  $E_{ep}$  is accomplished (in the form of elastic work on the target material) through the elastic-plastic boundary  $z_{ep}$ . Assuming that the elastic work is negligible compared to the kinetic energy of the penetrator ( $E_{ep} \approx 0$ ), the entire kinetic energy of the penetrator is deposited into the plastic work inside the control volume, which eventually results in generation of heat.



Inside the control volume, the distribution of the energy per unit volume is a function of the structure of the plastic flow field. As a first approximation, the total energy dissipated inside the control volume can be viewed as the volume of the plastic zone ( $\sim \Delta^3$ ) times a coefficient  $\kappa$ . The value of this coefficient characterizes the average dissipation of the energy per unit volume, and is a function of the structure of the plastic flow field and the target's strength. It follows then that since  $E_0 = \kappa \cdot \Delta^3$  (and since the energy  $E_0$  is fixed by the kinetic energy of the penetrator), the size of the plastic zone  $\Delta$  becomes one of the principle parameters that determine the resistance of the target to penetration.

The numerical experiments revealed that, depending on the particular structure of the employed constitutive model, the size of the plastic zone  $\Delta$  was either significantly affected by the model, or the effect was negligible. In particular, all numerical experiments with the constant yield-strength model resulted in approximately the same value of  $\Delta \approx 1.3$  cm, regardless of the value of the yield strength parameter  $Y$ . In contrast, a comparison between plots resulting from the constant yield-strength model ( $\Delta \approx 1.3$  cm) and pressure dependent yield-strength model ( $\Delta \approx 1.7$  cm) showed that a mere change in the target constitutive model resulted in a very significant 30% change in the size of the plastic zone.

In the previous approach, the target resistance to penetration is associated with the amount of energy per unit volume dissipated in the plastic flow. If the target is an ideal fluid, then, according to the ideal hydrodynamic theory of penetration (refs 24 and 25) the penetration resistance of the target is a function of the target density (i.e., inertia) only. If the target is a solid with a finite strength, the stronger the target the larger there must be the value of the energy dissipation per unit volume. In contradiction to this intuitive conclusion, the numerical experiments indicated the opposite: the higher the target resistance to penetration was, the larger was the size of the plastic zone  $\Delta$ , and therefore the average of the dissipated energy per unit volume,  $\kappa = E_0 / \Delta^3$ , was lesser. Explanation of these "contradictory" results needs a detailed analysis of the notion of the "target resistance to penetration."

### ANALYSIS OF THE AXIAL MOMENTUM BALANCE EQUATION ON THE LINE OF AXIAL SYMMETRY

Assuming that the penetration is approximately steady state, Pidsley (ref 5), and later Anderson and Walker (ref 7), showed that on the center line  $r=0$  the axial momentum balance equation 2b can be reduced to the following equation

$$\rho v_z \frac{dv_z}{dz} = \frac{d}{dz} (s_{zz} - p) + 2 \cdot \left. \frac{\partial s_{rz}}{\partial r} \right|_{r=0} \quad r=0, z_0 - l \leq z \leq z_{ep} \quad (18)$$

where  $l$  is the length of the penetrator and  $z_0$  and  $z_{ep}$  are axial coordinates of the target/penetrator interface and the elastic-plastic boundary, respectively. Consider an arbitrary

domain in the target  $z_0 \leq z \leq z^*$  ( $z^* \leq z_{ep}$ ), in which  $\rho = \rho_t(z)$ . The pressure at the target/penetrator interface can be found by integrating equation 18 over the interval  $[z_0, z^*]$ :

$$p(z_0) = \underbrace{\int_{z_0}^{z^*} \rho_t v_z dv_z}_{R_h} + p(z^*) + s_{zz}(z_0) - s_{zz}(z^*) - 2 \cdot \int_{z_0}^{z^*} \frac{\partial s_{rz}}{\partial r} \bigg|_{r=0} dz \quad (19)$$

The term  $R_h$  appearing on the right hand side of equation 19 represents the "hydrodynamic" component of the pressure at the target/penetrator interface, and assuming that the target material is incompressible (i.e.,  $\rho_t = \text{const}$ ), the integral can be evaluated easily.

In this work, concrete was modeled as a porous or "crushable" material, which has a significant "built-in" degree of compressibility. Based on the results of numerical experiments, it can be shown that the assumption of incompressibility can also be applied to this particular material model. In all cases studied, concrete was modeled employing the porous equation of state given by equations 5 to 7 in which the degree of the compressibility of this material is controlled primarily by the compaction pressure criterion, equation 5. Since the value of the concrete compaction pressure parameter  $p_c$  [ $p_c = 1.8$  Kbar (ref 15)] was greater than the value of the von Mises yield strength  $Y$  (or  $Y(p)$ ), the calculated zones of crushed concrete were inside the domain of the plastic zone,  $z_0 \leq z \leq z_{ep}$ . Numerical experiments showed (ref 8) that once the concrete is crushed and the porosity  $\phi$  is "squeezed out," the changes in the density of the crushed concrete become negligible. Thus, assuming that the coordinate  $z^*$  is within this region of completely crushed concrete (with  $\rho_t \approx \text{const}$ ), the term  $R_h$  of equation 19 can be integrated, which results in the following

$$p(z_0) \approx \frac{1}{2} \rho_t v_z^2(z^*) - \frac{1}{2} \rho_t v_z^2(z_0) + p(z^*) + \underbrace{s_{zz}(z_0) - s_{zz}(z^*)}_{\Delta s_{zz}} - \underbrace{2 \cdot \int_{z_0}^{z^*} \frac{\partial s_{rz}}{\partial r} \bigg|_{r=0} dz}_{R_s} \quad (20)$$

In general, determination of the parameters  $v_z(z=z_0, z^*)$ ,  $p(z^*)$ ,  $s_{zz}(z=z_0, z^*)$ , and  $s_{rz,r}(z)$  requires numerical solution of the system of equation 1 to 3. However, in the case of an axially symmetrical plastic flow, a closed form analytical solution for the deviatoric stress  $s_{zz}$  can be found on the center line  $r=0$ . In the case of the von Mises yield criterion, equation 8 to 10, the stress deviatoric tensor is given by the following flow rule

$$s_{ij} = \frac{k \dot{\epsilon}_{ij}}{\sqrt{I}} \quad (21)$$

where  $\dot{\epsilon}_{ij}$  is the strain rate tensor. The strain rate parameter  $I$  is given by the following equation

$$I = \frac{1}{2}(\dot{\epsilon}_{rr}^2 + \dot{\epsilon}_{\theta\theta}^2 + \dot{\epsilon}_{zz}^2) + \frac{1}{4}(\dot{\gamma}_{\theta z}^2 + \dot{\gamma}_{zr}^2 + \dot{\gamma}_{r\theta}^2) \quad (22)$$

Let's evaluate  $\dot{\epsilon}_{ij}$  and  $I$  on the center line  $r=0$ . Since the considered plastic flow field is axially symmetric,  $v_{z,r}=v_{r,z}=v_{r,q}=v_{q,z}=v_{z,q}=0$ . It follows then that at  $r=0$

$$\dot{\epsilon}_{rr} = \dot{\epsilon}_{\theta\theta} = \left. \frac{\partial v_r}{\partial r} \right|_{r=0} = 0 \quad (23a)$$

$$\dot{\gamma}_{\theta z} = 0 \quad (23b)$$

$$\dot{\gamma}_{r\theta} = 0 \quad (23c)$$

$$\dot{\gamma}_{zr} = 0 \quad (23d)$$

Substituting equations 23 b to d into equations 21 and 22 results in the following

$$s_{\theta z} = s_{zr} = s_{r\theta} = 0 \quad (24)$$

$$I = \frac{1}{2}(\dot{\epsilon}_{rr}^2 + \dot{\epsilon}_{\theta\theta}^2 + \dot{\epsilon}_{zz}^2) \quad (25)$$

Assumption that the target material is incompressible permits significant simplification of the equation for the parameter  $I$ . Consider a perfectly incompressible material for which the following equation holds

$$\dot{\epsilon}_{rr} + \dot{\epsilon}_{\theta\theta} + \dot{\epsilon}_{zz} = 0 \quad (26)$$

Substituting equation 23a into equation 16 results in:

$$\dot{\epsilon}_{rr}|_{r=0} = \dot{\epsilon}_{\theta\theta}|_{r=0} = -\frac{1}{2} \dot{\epsilon}_{zz}|_{r=0} \quad (27)$$

Thus,

$$I = \frac{3}{4} \dot{\epsilon}_{zz}^2 \quad @ \ r=0 \quad (28)$$

$$s_{zz} = \frac{2k}{\sqrt{3}} \quad @ \ r=0 \quad (29)$$

It is interesting to note that equation 29 can be useful for numerical validation of computer codes for axially symmetric plastic flow analysis. The profiles of deviatoric stresses  $s_{zz}$  shown in figure 6a are based on a numerical solution of equations 1 to 3 using the CALE code (ref 1) and are in excellent agreement with the closed form analytical predictions, equation 29.

In the case of the constant yield-strength model, equation 29 results in

$$\Delta s_{zz} = 0 \quad (30)$$

In the case of the pressure dependent yield-strength model,  $k(p) = Y(p)/\sqrt{3}$

$$\Delta s_{zz} = \frac{2}{3} [Y(p(z_0)) - Y(p(z'))] \quad (31)$$

Assuming that above the compaction pressure limit  $p_c$ , the strain-hardening of concrete is insignificant [i.e.,  $dY/dp$  is relatively small (fig. 4)], equation 31 results in  $\Delta s_{zz} \approx 0$ .

Figure 7 compares various terms of equation 20. Since the contribution of the deviatoric stress term  $\Delta s_{zz}$  is either zero or negligible, the term  $\Delta s_{zz}$  is not shown in the figure. Unfortunately, a closed form analytic solution for the radial derivative of the shear stress deviator  $s_{rz,r}|_{r=0}$  is not available. The shear stress deviator term  $R_s$  can be evaluated numerically based on the results of the numerical experiments. The calculated profiles of the radial derivative of the shear stress deviator  $s_{rz,r}$  along the center line  $r=0$  are shown in figure 6b. Although one can intuitively surmise that changes in the constitutive model significantly affect the deviatoric stress, the results of the analysis shown in figure 7 indicate that the relative changes in the magnitude of the shearing deviatoric stress term  $R_s$  are rather negligible.

Comparison between the relative magnitudes of terms of equation 20 shows that the terms that contribute the most to the target/penetrator interface pressure are the pressure term  $p(z')$  and the "hydrodynamic" term,  $0.5\rho_t[v_z^2(z') - v_z^2(z_0)]$ . As discussed in the previous section, during the high velocity penetration, the pressure in the target material fluctuates rapidly and within rather wide limits. These rapid and large fluctuations prohibit establishing a direct relationship between the target constitutive modeling and the pressure terms  $p(z_0)$  and  $p(z')$ , unless the instantaneous values of  $p(z_0)$  and  $p(z')$  (fig. 7) are time averaged.

In contrast to the pressure term  $p(z')$ , the "hydrodynamic" term (which represents the kinetic energy of the target material), is not susceptible neither to large nor to rapid fluctuations, which makes it a convenient parameter for examining effects of the target constitutive modeling.

In order to establish the physical meaning of the "hydrodynamic" term  $R_h$ , it is instructive to compare equations 19 and 20 with the equation for the pressure at the target/penetrator interface given by the modified hydrodynamic theory of penetration, equation 13. Comparison between equations 13 and 19 indicates that these equations are identical provided that

$$\frac{1}{2} \rho_{t0} u^2 = - \int_{z_0}^{z^*} \rho_t v_z dv_z \quad (32)$$

$$R_t = -[\rho(z^*) + s_{zz}(z_0) - s_{zz}(z^*) - 2 \cdot \int_{z_0}^{z^*} \frac{\partial s_{rz}}{\partial r} \Big|_{r=0} dz] \quad (33)$$

The definition of pressure employed in equation 20 implies that the pressure is negative. However, according to equation 13,  $p \geq 0$ , which makes it necessary to introduce a minus sign on the right hand sides of equations 32 and 33. It follows then that the idealized penetration rate  $u$ , per modified hydrodynamic theory of penetration, is given by

$$u = \left[ \frac{2}{\rho_{t0}} \int_{z_0}^{z^*} \rho_t v_z dv_z \right]^{\frac{1}{2}} \quad (34)$$

Assuming that the target material is incompressible, the idealized penetration rate  $u$  is given simply by

$$u \approx \left[ \frac{\rho_t}{\rho_{t0}} [v_z^2(z_0) - v_z^2(z^*)] \right]^{\frac{1}{2}} \quad (35)$$

According to the modified hydrodynamic theory of penetration, increases in the strength factor  $R_t$  decrease the penetration rate  $u$ . Similarly, one can expect that the constitutive modeling changes, resulting in increases in the target resistance to penetration, have to decrease the idealized penetration rate  $u$ . This hypothesis can be supported by the following results. The numerical experiments showed that in the case of the constant yield-strength model, the idealized penetration rate was  $u' = 0.123$  cm/ $\mu$ s. However, after the employed constitutive model was changed to the pressure-dependent yield-strength model (which increased the target resistance to penetration), the idealized penetration rate was decreased to  $u'' = 0.121$  cm/ $\mu$ s. Because the relative change in the magnitude of the penetration rate is very small, the accuracy of these predictions will be addressed in the following section.

The calculated trajectories of the front and the rear of the penetrator for the constant yield-strength and the pressure dependent yield-strength models are shown in figure 8.

Numerical experiments with the constant yield-strength model showed that the analysis was not affected by the value of the von Mises yield parameter  $Y$ , which resulted in identical trajectories for all cases studied. However, changing the employed constitutive model to the pressure-dependent yield-strength model, resulted in a slight decrease of the slope of the trajectory of the penetrator front, while the trajectory of the penetrator rear remained unchanged. The significance of this result is as follows.

The slopes of the trajectories of the penetrator front and the rear represent the penetration rate  $u$  and the penetrator rigid body velocity  $v$ , respectively. According to the modified hydrodynamic theory of penetration, the penetrator erosion rate is given by

$$\frac{dl}{dt} = - (v - u) \quad (36)$$

where  $l$  is the instantaneous length of the penetrator. Numerical experiments showed that, after the concrete constitutive model was changed to the pressure-dependent yield-strength model, the penetration rate  $u$  was decreased. Since the rigid body velocity  $v$  remained unchanged, the absolute value of the penetrator erosion rate  $|dl/dt|$  was increased proportionally. According to the hydrodynamic theory of penetration, the penetration is accomplished at the expense of the penetrator material. Therefore, the faster the penetrator erodes, the faster it consumes the available kinetic energy which, finally, results in a decrease in the penetration. This is precisely the reason why the pressure-dependent yield-strength model resulted in a decrease in the penetration depth. Thus, it is reasonable to relate the notion of target resistance to penetration rate  $u$ , and not to the pressure at the target/penetrator interface  $p(z_0)$ , nor to strength related parameters such as  $R_s$  or  $\Delta s_{zz}$ .

## THE EFFECT OF THE TARGET CONSTITUTIVE MODELING

Let us first examine the effect of the target constitutive modeling on the axial component of the velocity  $v_z$ . The calculated profiles of the axial component of velocity  $v_z$  along the center line  $r=0$ , at time  $t=35 \mu s$  after the impact, are shown in figure 9. Note, that all curves are approximately "parallel" to each other, and that increases in the "spacing" between the curves correlate very well with increases in the target resistance to penetration. Comparison among the curves shows that the target/penetrator interface velocities  $v_z(z_0)$  differ from each other very little. Because the accuracy of assessing values of  $v_z(z_0)$  is limited by the resolution of the computational mesh, the effect of the target constitutive modeling on the target/penetrator interface velocity can be examined more conveniently by employing a concept of the idealized penetration rate  $u$ , given by equations 34 and 35.

As discussed in the preceding section, after the target constitutive model was changed from the constant yield strength to the pressure-dependent yield strength, the resulting idealized penetration rate was reduced by a relatively small value of  $\Delta u = u' - u'' = 0.002 \text{ cm}/\mu\text{s}$ . The accuracy of this prediction in the reduction of the idealized penetration rate can be proved by results of numerical experiments. Assuming that the penetration process is a steady-state one, after  $t = 35 \mu\text{s}$ , the difference in penetration rates of  $\Delta u = 0.002 \text{ cm}/\mu\text{s}$  produces a difference between the axial positions of the target/penetrator interfaces of  $\Delta z_0 \approx \Delta u \cdot t = 0.07 \text{ cm}$ , which agrees with the results shown in figure 9. Note, that in the case of the constant yield-strength model, the "spacing" between the curves increases consistently with increases in the von Mises yield-strength parameter  $Y$ , resulting in relatively small axial "shifts" of the  $v_z$ -curves. In the case of the pressure-dependent yield-strength model the "shift" of the curve is the largest, which implies a relatively significant decrease in the penetration rate.

One should also note that, although all curves shown in figure 9 are approximately "parallel", on the interval  $[z_0, z^*]$  their slopes are slightly different, which is related to the differences in the target resistance to penetration. Compared with the slopes resulting from calculations with the constant yield-strength model, the change to the pressure-dependent yield-strength model produced a rather significant decrease of the "average" slope  $dv_z/dz$  (on the interval  $[z_0, z^*]$ ). Since the numerical experiments showed that regardless of the employed constitutive model  $\rho_t(z)$  profiles are identical, the results shown in figure 9 are in complete agreement with equation 34, which predicts that the idealized penetration rate  $u$  is proportional to the area under the curve  $f(z) = \rho_t v_z$ .

In the proceeding section we established that the target resistance to penetration is directly related to the penetration rate  $u$ . It would be instructive to examine the structure of the term  $R_h$ . Rearranging terms of equation 19 results in the following equation

$$R_h = \frac{1}{2} \rho_{t0} u^2 = \underbrace{p(z_0) - p(z^*)}_{\Delta p} + \underbrace{s_{zz}(z^*) - s_{zz}(z_0)}_{-\Delta s_{zz}} + \underbrace{2 \int_{z_0}^{z^*} \frac{\partial s_{rz}}{\partial r} dz}_{-R_s} \quad (37)$$

Since changes in the target constitutive modeling have a negligible effect on the terms  $\Delta s_{zz}$  and  $R_s$ , it follows then that changes in the penetration rate  $u$  are affected mostly by changes in the pressure gradient  $\Delta p$ . Thus, the target resistance to penetration should increase with decreases in the pressure gradient  $\Delta p$ .

As discussed in the preceding section, rapid and large pressure fluctuations, which are usually present in the numerical analysis of the high velocity penetration, are due to the interference of the stress waves. Since the penetration process is a steady state one, and since for the conditions considered the stress wave propagation speeds are approximately constant, the spatial gradients of the pressure waves should be relatively stable. This can



be clarified by an example of surface waves in a liquid. For a stationary observer, fluctuations in the height of surface waves are rather significant, while in the reference frame that moves at the speed of the wave, the shape of the waves stays approximately the same. In the case of high velocity penetration, numerical experiments show that, although pressure profiles may slightly vary with time, their shapes are similar and, therefore, "average" spatial gradients  $dp/dz$  are relatively stable regardless of the employed constitutive model. Figure 10 shows calculated profiles of the pressure  $p$  along the center line  $r=0$ , at time  $t=35$   $\mu$ s after impact. Similar to the decreases in slopes of the  $v_z$ -curves, the shapes of pressure profiles show that decreases in the slopes  $dp/dz$  correlate very well with increases in the target resistance to penetration. Thus, the results of the numerical experiments are in complete agreement with the predictions of equation 37, which states that the penetration rate is proportional to the pressure gradient  $\Delta p$ .

This general tendency (i.e., that the gradients of plastic flow field variables consistently diminish with increases in the target resistance to penetration) is related to increases in the size of the plastic zone discussed in the preceding section and shown in figure 2. The nature of the relationship between the gradients of the flow field variables and the extent of the plastic zone is as follows: numerical experiments show that the changes in the target constitutive modeling do not significantly affect plastic flow field variables neither at the target/penetrator interface  $z_0$ , nor at the elastic-plastic boundary  $z_{ep}$ . It follows then that, since inside the plastic zone  $z_0 \leq z \leq z_{ep}$  flow field variables change monotonically, once the extent of the plastic zone  $\Delta = z_{ep} - z_0$  is increased, the gradients of flow field variables  $dg(z)/dz \sim \Delta g(z)/\Delta$  are decreased proportionally to increases in  $\Delta$ .

A brief comment is needed on the pressure discontinuity in the vicinity of  $z=z^*$  (fig. 10). As discussed in the previous section, the employed numerical model attempted to model the behavior of the break gages. The results of numerical experiments show that during a high velocity penetration, the behavior of thin copper sheets surrounded by "crushable" concrete is similar to the behavior of a flexible membrane restraining a compressible continuum. In agreement with this analogy, the numerical analysis shows that across the thickness of a break gage the pressure changes very rapidly, which results in a "jump" from the pressure build-up "inside" the zone of completely crushed concrete to the "ambient" pressure "outside" of this zone. Small differences in the axial positions of the break gages are due to the differences in the target resistance to penetration. The higher the target resistance to penetration, the smaller was the displacement of the break gage.

At this point, it is appropriate to address experimental results on measuring the size of the plastic zone in the front of the penetrator. The technique for measuring the plastic zone size in the front of the penetrator is based on comparison between the calculated trajectory of the penetrator front and the experimental data from trigger times of the break gages. The results of this comparison are shown in figure 8. Assuming that "breaks" in gages occurred approximately at the time when the elastic-plastic boundary reached the gages, comparison between the linear regression of the experimental data and the trajectory of the penetrator front results in the size of the plastic zone of  $\Delta_{exp} \approx 1.3$  cm. This value of the



plastic zone size agrees with the predictions based on calculations with the constant yield-strength model [ $\Delta \approx 1.3$  cm (fig. 2a)] but disagrees with the predictions resulting from the analysis with the pressure-dependent yield-strength model [ $\Delta \approx 1.7$  cm (fig. 2b)].

As shown in figure 8, the trigger time data are scattered, which may be due to a number of reasons including inhomogeneities in concrete, the uncertainty in the mode of the gage failure, etc. It should be noted that the deviation of the trigger time data (with respect to their linear regression) is approximately of the same order as the discrepancy between  $\Delta_{exp} = 1.3$  cm,  $\Delta = 1.3$  cm, and  $\Delta = 1.7$  cm. Therefore, with the present degree of accuracy, this technique can not be applied for proving the validity of either of the constitutive models studied, based on the experimental data of the plastic zone size. Previously, the break gage technique was successfully used for validation of the concrete equation of state modeling, and showed that the "porous" equation of state model is the most realistic for representing the elastic-plastic flow in concrete medium resulting from the high velocity penetration (ref 8). Extension of this technique to problems related to the concrete constitutive modeling would require a number of improvements which ought to reduce the amount of scatter in the trigger time data. This can be accomplished in a number of ways such as improving the homogeneity of concrete (in the vicinity of the break gages), refining the gage design (to exclude the uncertainty in the gage failure mechanism), etc.

Another important penetration parameter that is significantly affected by the target constitutive modeling is the radial component of velocity,  $v_r$ . Profiles of  $v_r$  at a distance of approximately 0.7 cm in the front of the target/penetrator interface, at  $t = 35 \mu s$  after impact, are shown in figure 11. Comparison between these curves shows that with increases in the target resistance to penetration, the radial component of the velocity is consistently decreasing. The effect of this parameter on the formation of the crater is as follows.

According to the cavity-expansion theory (e.g., ref 26), the motion of the target material can be viewed as a continuous expansion of a series of imaginary cavities which initially have zero radius and then expand to a size that permits passage of the penetrator. When the impact velocities are sufficiently high, the penetrator nose deforms into a characteristic mushroom-like shape. Behind the mushroom, the hole continues to grow under the inertial forces that are due to the radial motion of the target material. The magnitude of these forces is determined by the intensity of the target material flow at the penetrator mushroom. The smaller the radial component of the velocity, the smaller are the inertial forces, and, therefore, the smaller are the resulting crater diameters.

Another important parameter that determines the final hole diameter is the size of the plastic zone behind the penetrator mushroom. Numerical experiments showed (fig. 5) that after the target constitutive model was changed to the pressure-dependent yield-strength model, the extent of the plastic zone in the target was increased not only in front of the penetrator but also behind the penetrator mushroom. Increases in the plastic zone size increase the degree of the viscous dissipation of the energy (which through plastic work is converted to heat) stored in the expanding hole. Thus, the increase in the plastic zone size

combined with the decrease in the radial velocity profile resulted in a significant decrease in the final crater diameter shown in figure 2.

## CONCLUSIONS

1. Analysis of the time average pressure at the interface between the penetrator and the target shows that, in an agreement with the hydrodynamic theory of penetration, the interface pressure increases with increases in the "target strength," a tendency that may be intuitively associated with the effect of the von Mises yield strength  $k$  or  $k(p)$ . However, calculations show that in the case of the pressure-dependent yield model (the "average" yield is approximately 1.6 Kbar), the time averaged pressure at the projectile/target interface is higher than the pressure resulting from the 1.8 Kbar constant yield model. It follows then that the target resistance to penetration is not related simply either to the pressure or to the yield strength alone.
2. The size of the plastic zone in front of the penetrator was shown to be directly related to target resistance to penetration. The numerical experiments with different constitutive models showed that, depending on the particular structure of the employed model, the size of the plastic zone  $\Delta$  was either significantly affected by the model or the effect was negligible. In particular, all numerical experiments with the constant yield-strength model resulted in approximately the same value of  $\Delta \approx 1.3$  cm, regardless of the value of the yield strength parameter  $Y$ . However, a change in the target constitutive model from the constant yield-strength model to the pressure-dependent resulted in a very significant 30% change in the size of the plastic zone ( $\Delta = 1.7$  cm).
3. Analysis of the results of the numerical experiments showed that the penetration rate  $u$  is the principle parameter that is directly related to the target resistance to penetration. Since the rigid body velocity  $v$  is not significantly affected by the changes in  $u$ , the penetrator erosion rate increases proportionally to decreases in the penetration rate. The faster the penetrator erodes, the faster it consumes the available kinetic energy, which ultimately results in a decrease of the penetration.
4. Detailed analysis of the plastic flow field at the center line showed that the penetration rate  $u$  is directly proportional to the pressure gradient  $\Delta p$ . Numerical experiments showed that changes in the target constitutive modeling do not significantly affect plastic flow field variables neither at the target/penetrator interface  $z_0$ , nor at the elastic-plastic boundary  $z_{ep}$ . Given that inside the plastic zone  $z_0 \leq z \leq z_{ep}$  flow field variables change monotonically, once the extent of the plastic zone  $\Delta = z_{ep} - z_0$  is increased, the gradients of flow field variables  $dg(z)/dz \sim \Delta g(z)/\Delta$  are decreased proportionally to increases in  $\Delta$ . Therefore, the larger the size of the plastic zone  $\Delta$ , the slower is the penetration rate  $u$ , and the higher is the target resistance to penetration.

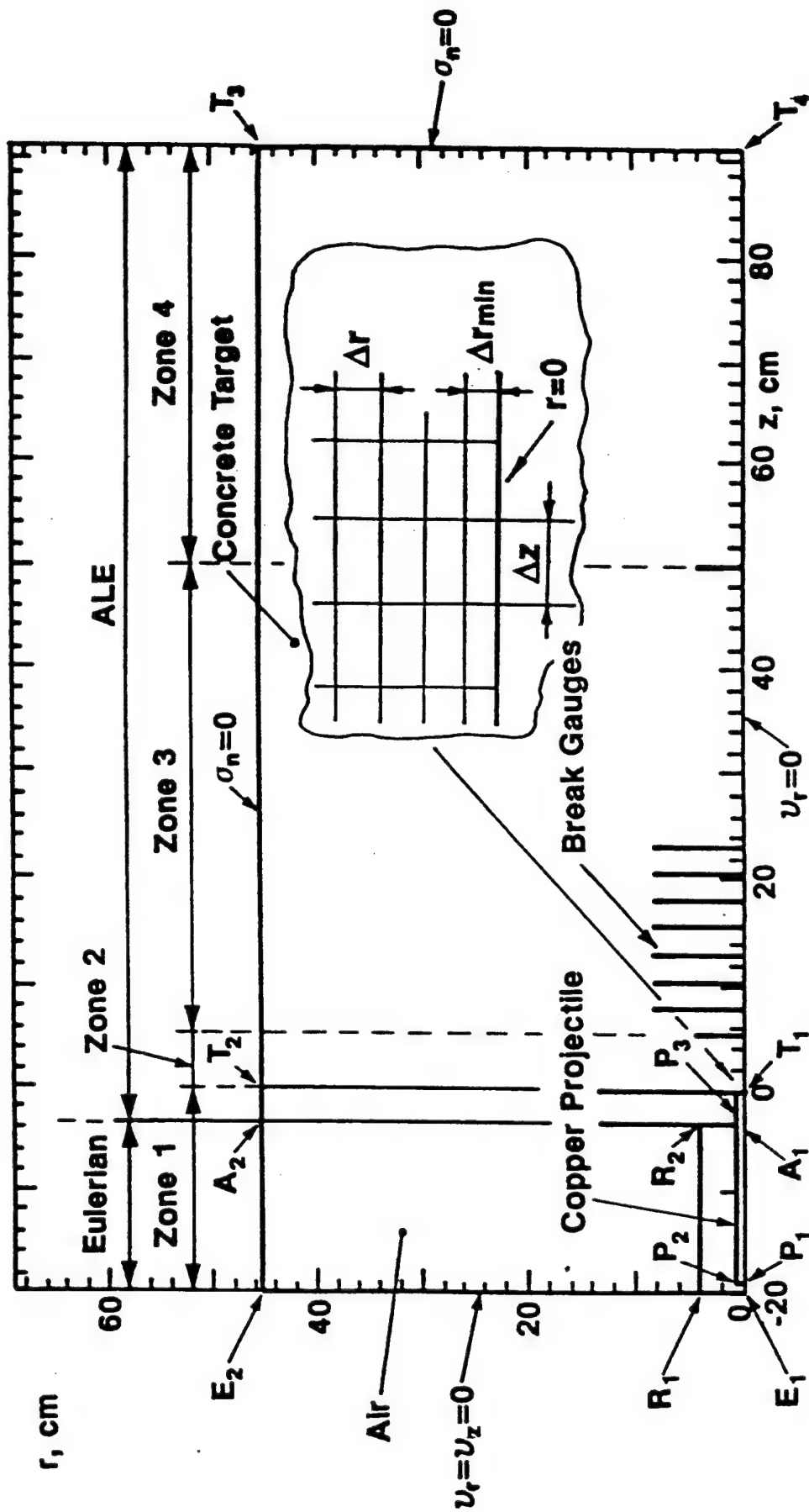


Figure 1  
Initial configuration of the computational domain: spherical-nose copper projectile impacting a right circular cylinder of concrete with velocity  $V_0 = 0.1835$  cm/ $\mu$ s

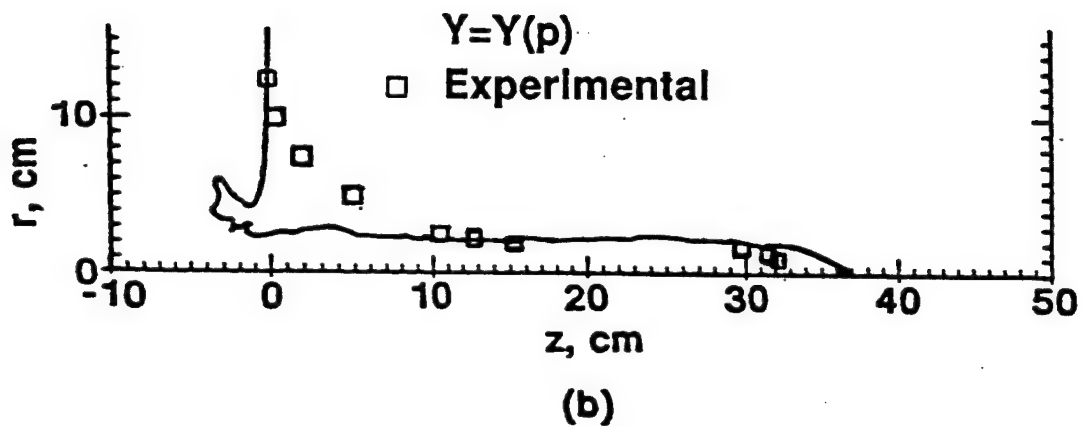
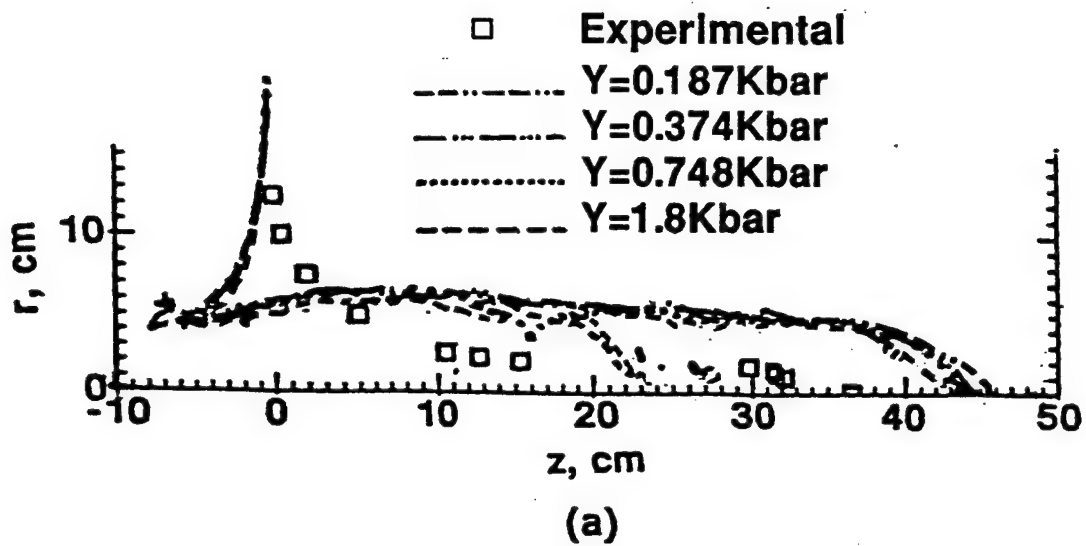


Figure 2  
Resulting hole profiles employing (a) the constant yield-strength model and (b) the pressure dependent yield-strength model. Experimental data reference1.

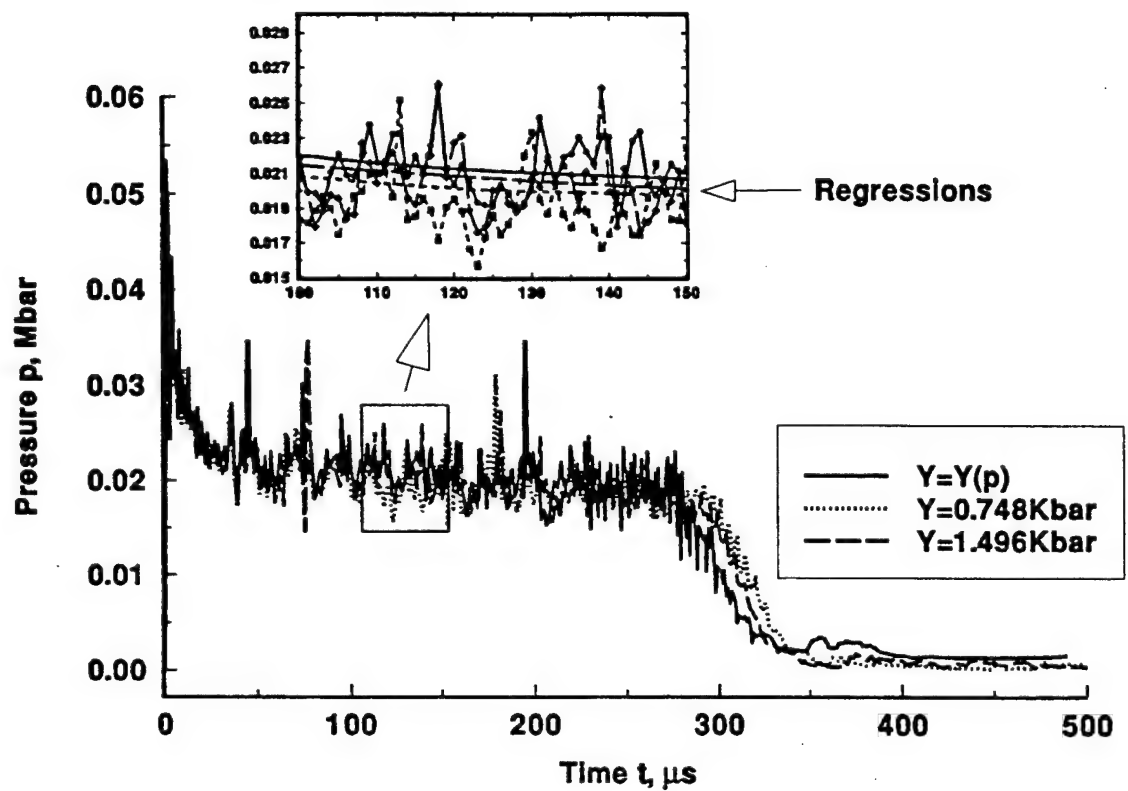


Figure 3  
History of pressure  $p=p(t)$  at the target/penetrator interface at  $r=0$  for various constitutive models

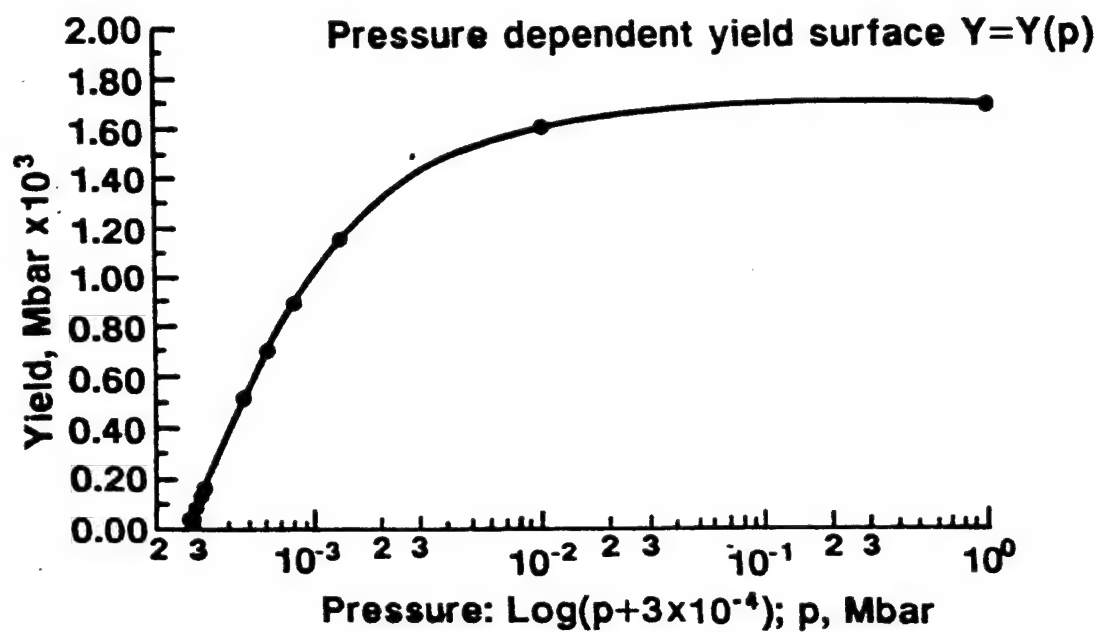


Figure 4  
Empirical yield strength function  $Y=Y(p)$  for the pressure dependent  
yield-strength model (ref 16)

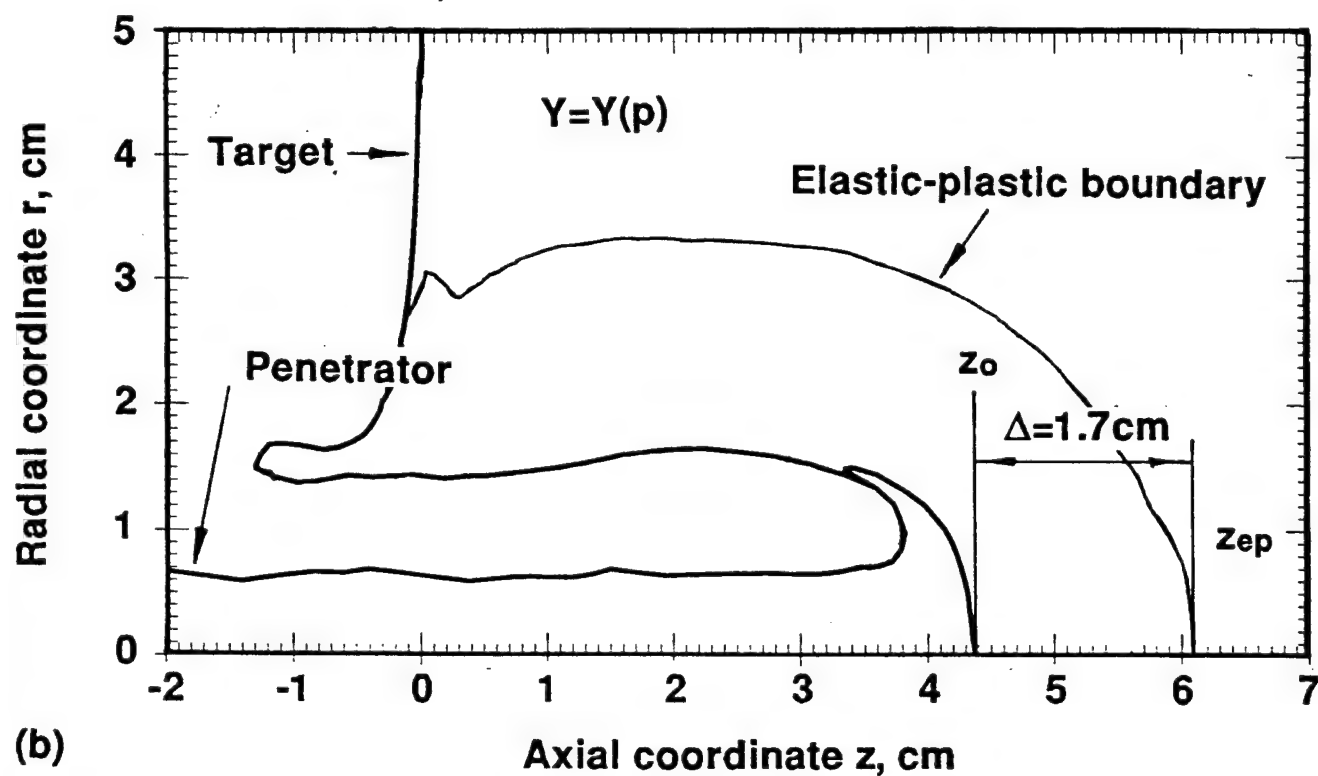
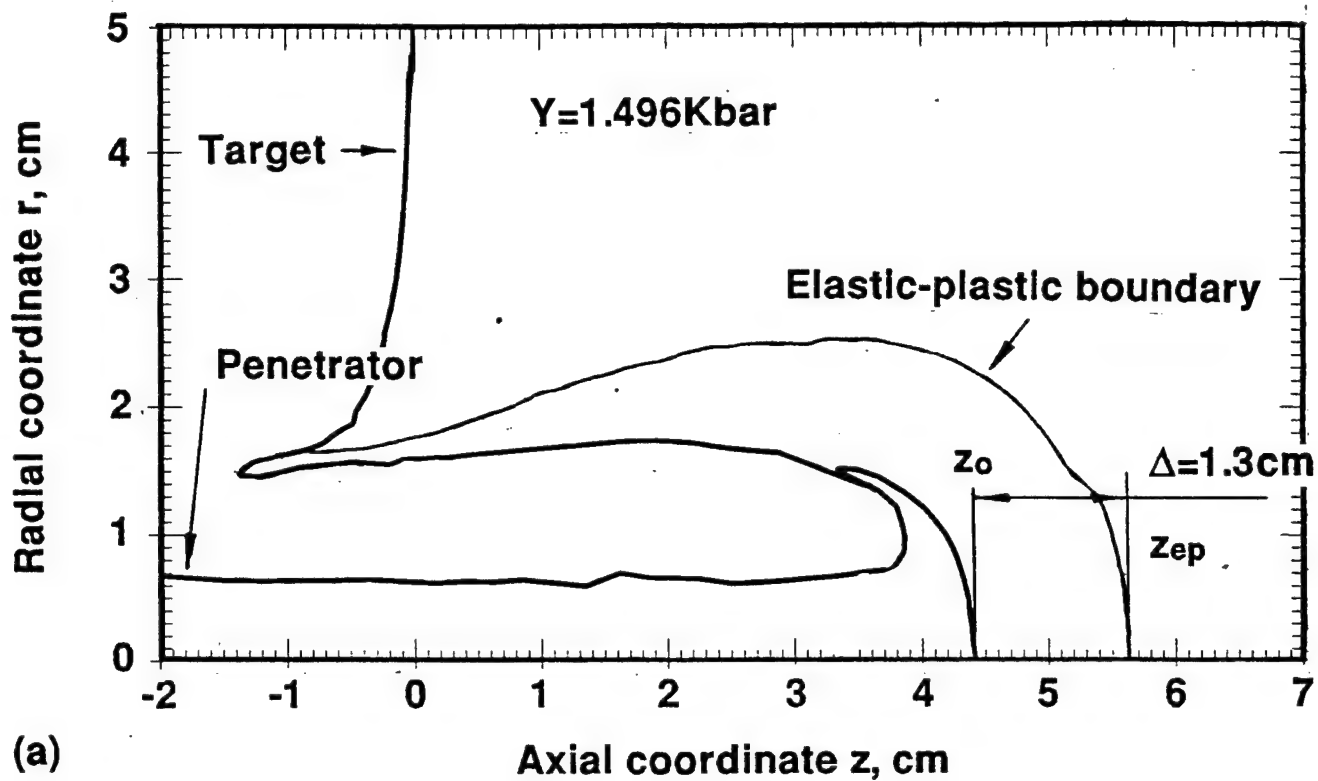


Figure 5  
Structure of the elastic-plastic flow field in target (time  $t=35\mu\text{s}$ ,  $\gamma=0.062$ )

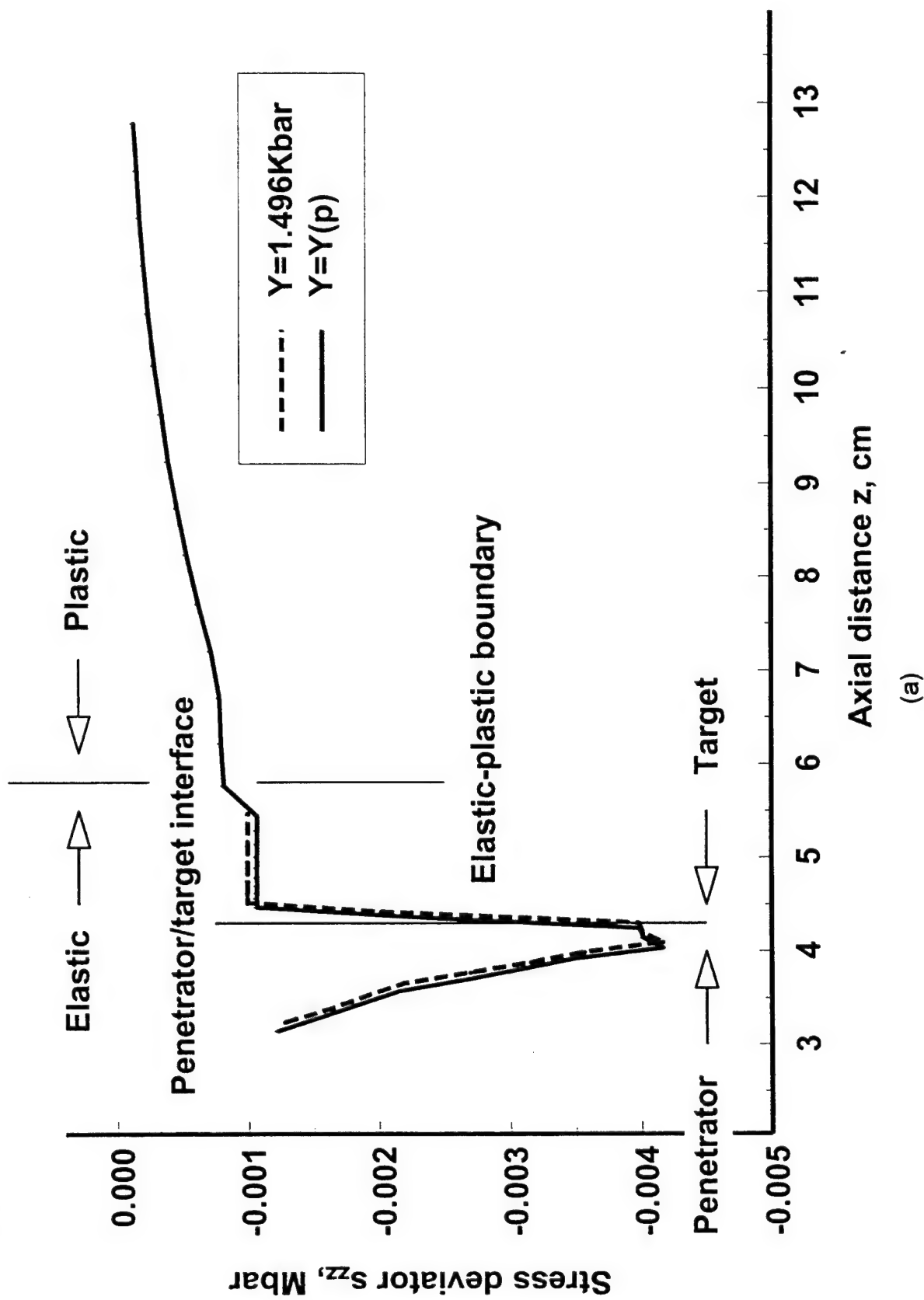
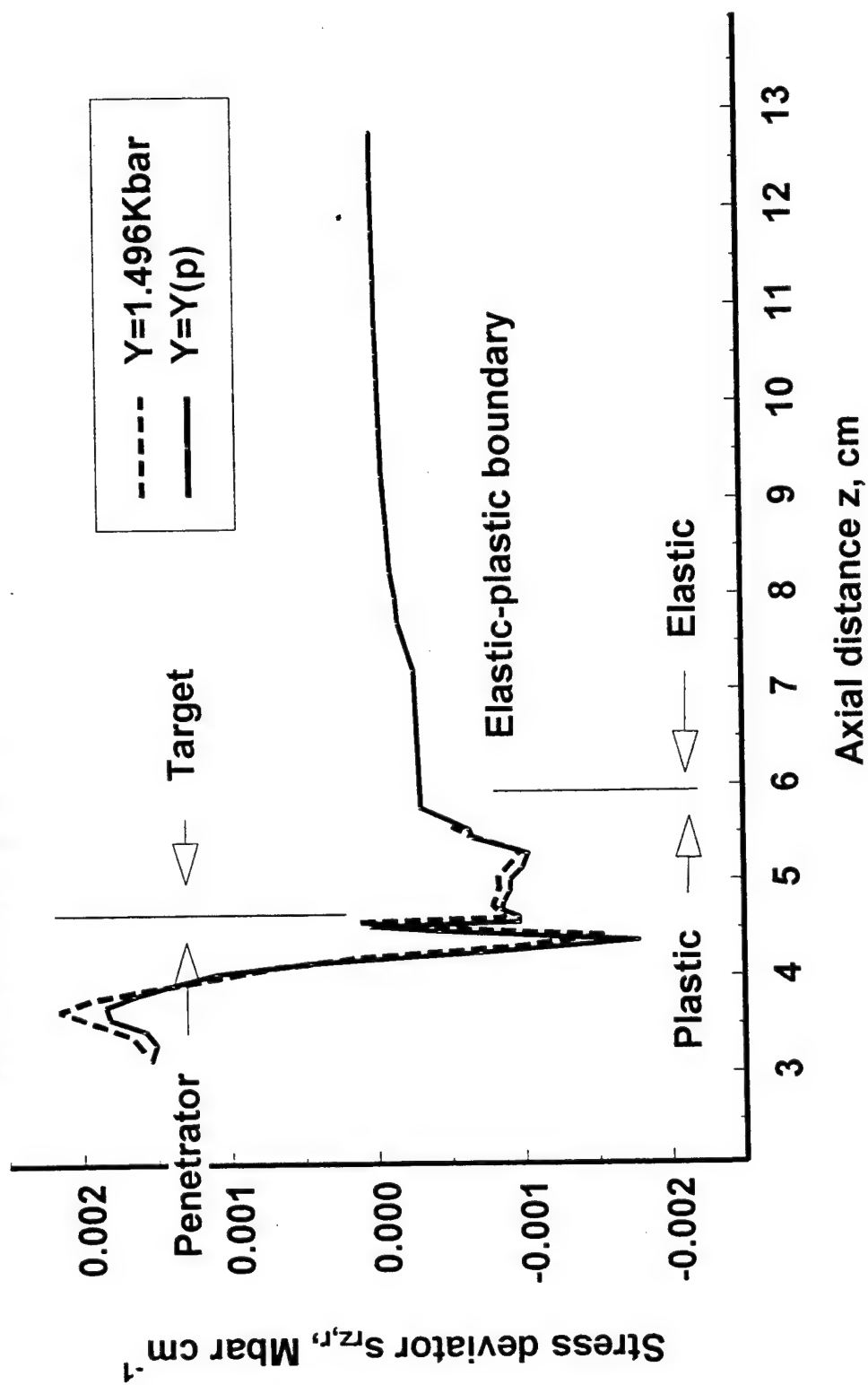


Figure 6  
 Calculated profiles of (a)  $s_{zz}$  and (b)  $s_{rz}$  along the center line  $r=0$  for the constant yield-strength and the pressure dependent yield-strength models ( $t=35 \mu\text{s}$ )



Penetrator/target interface



(b)

Figure 6  
(cont)

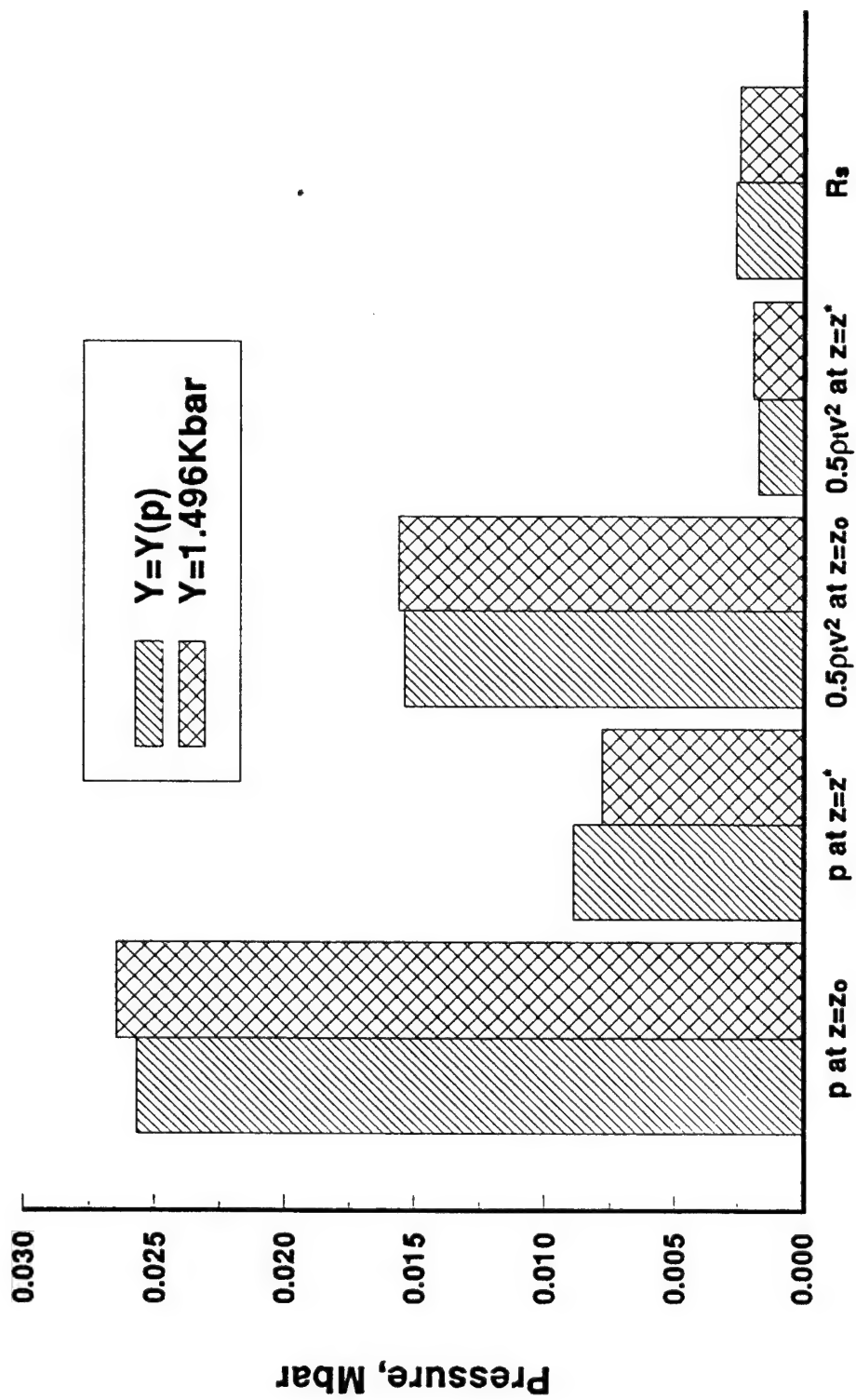


Figure 7  
Comparison between the instantaneous values of various terms comprising the pressure at the target/penetrator interface ( $t=35 \mu s$ )

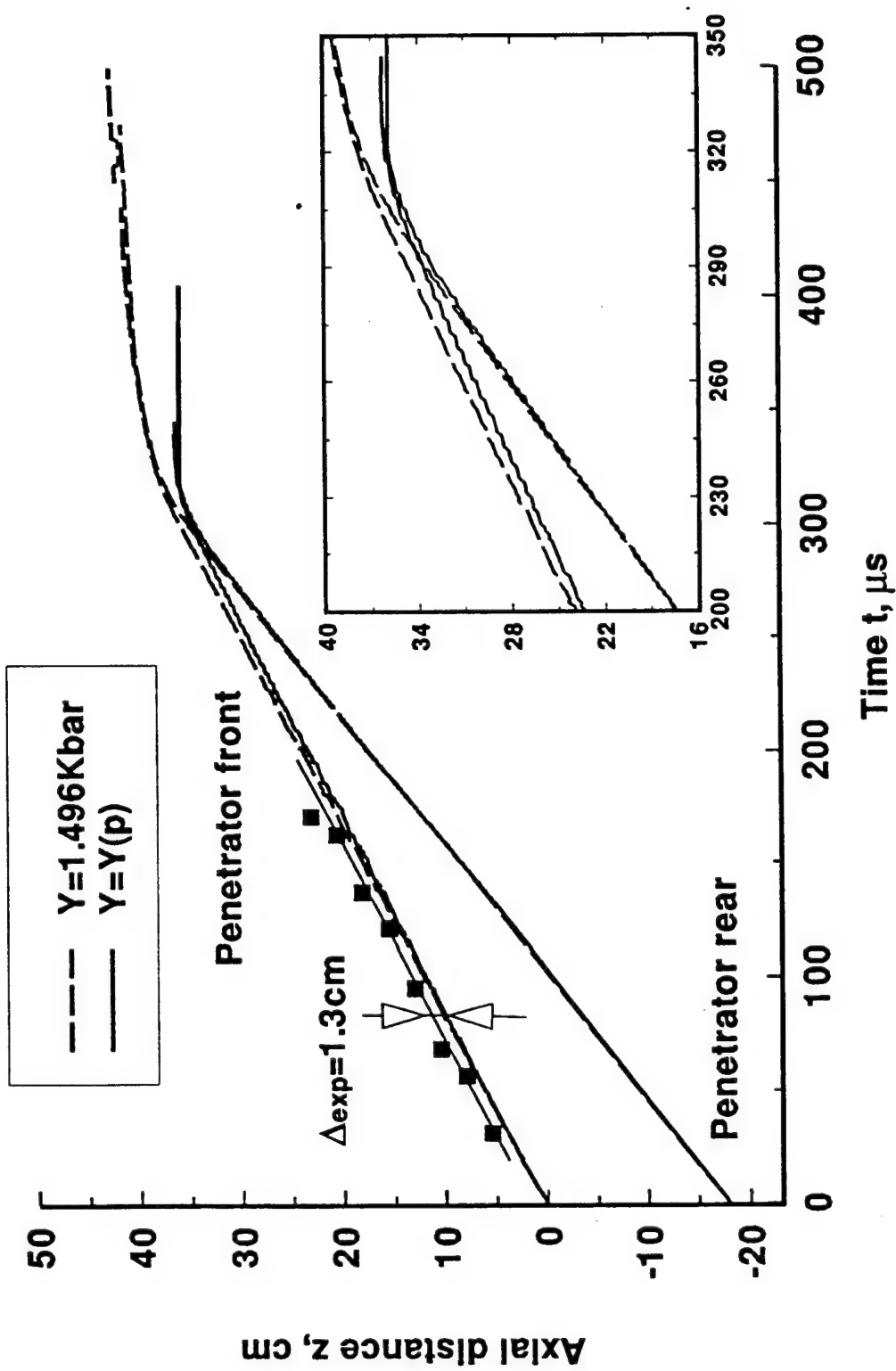


Figure 8  
Trajectories of the front and the rear of the penetrator for the constant yield-strength and the pressure dependent yield-strength models. Experimental data reference 8.

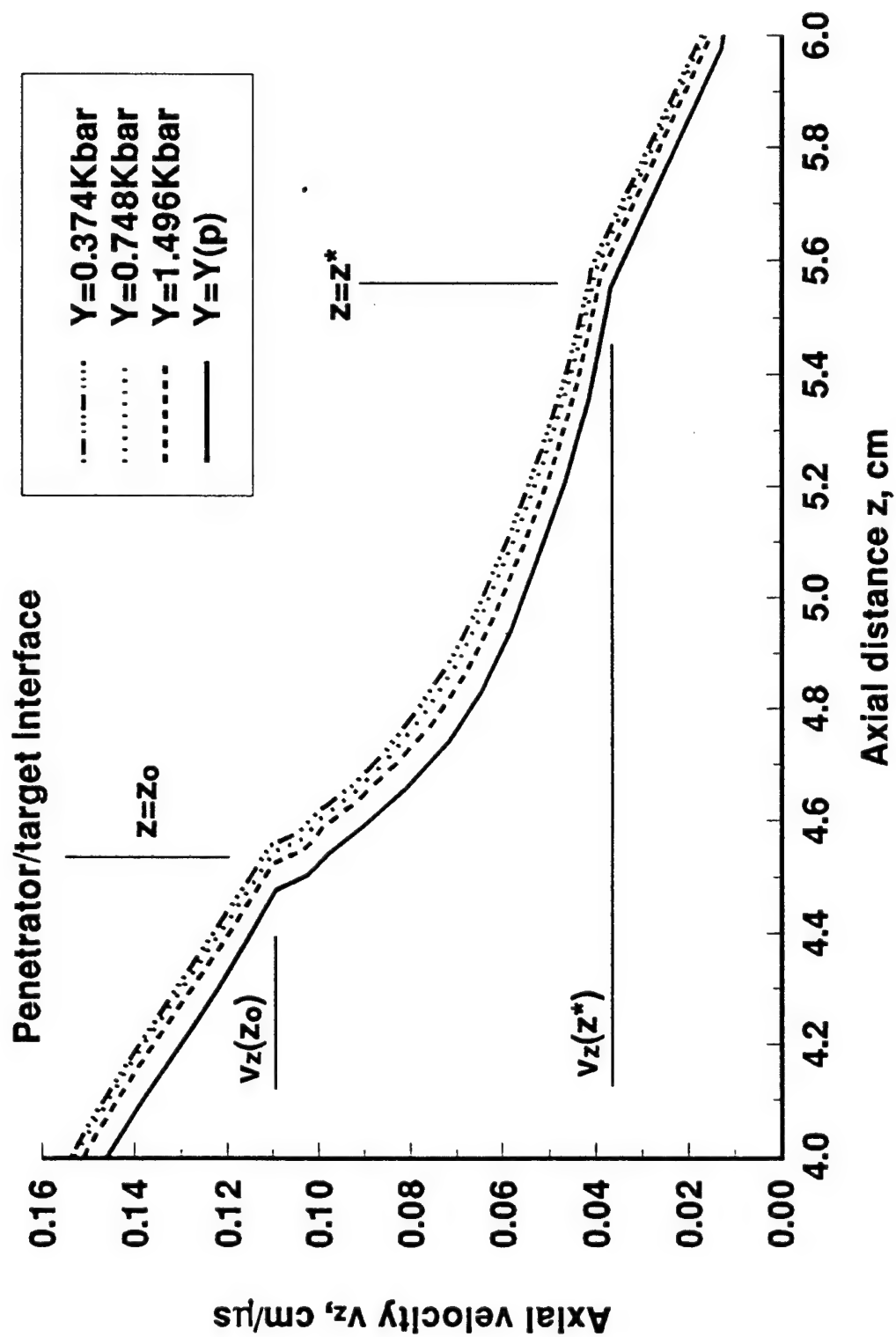


Figure 9  
Calculated profiles of the axial component of velocity  $v_z$  at the center line  $r=0$  ( $t=35 \mu\text{s}$ )

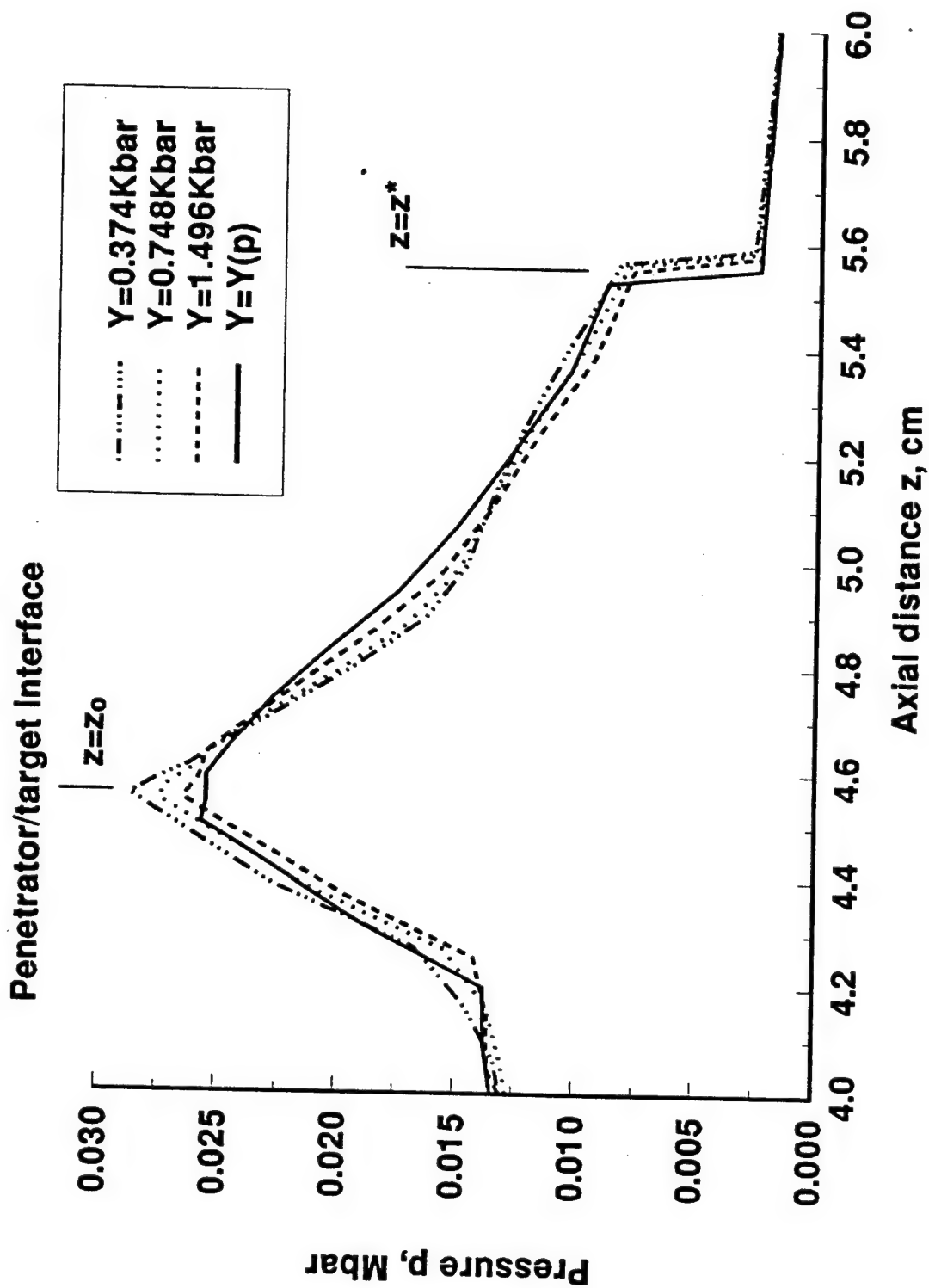


Figure 10  
Calculated profiles of pressure  $p$  along the center line  $r=0$  ( $t=35\text{ }\mu\text{s}$ )

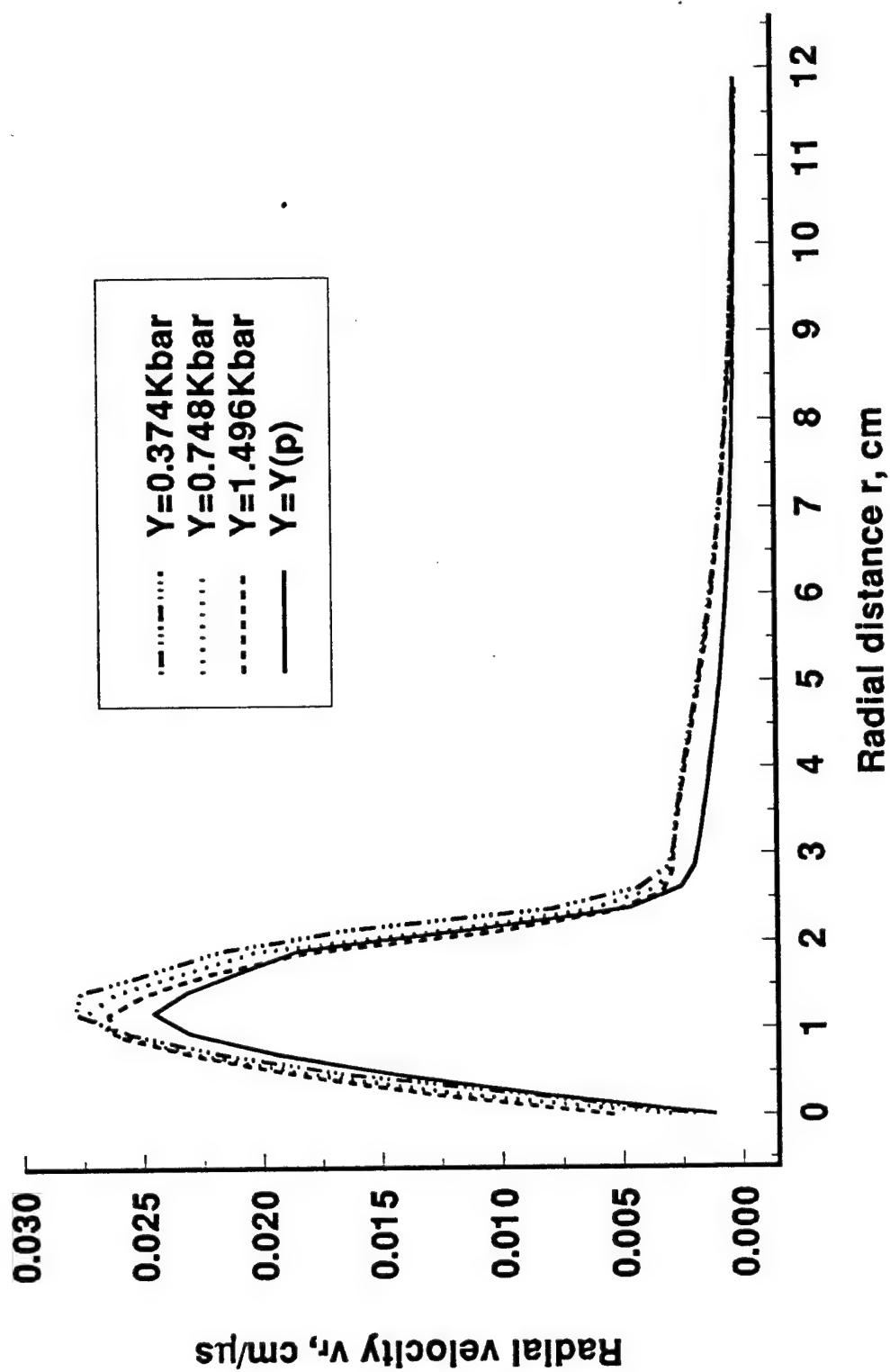


Figure 11  
Profiles of the radial velocity component  $v_r$  versus radial coordinate  $r$  ( $z=5.2 \text{ cm}$ ,  $t=35 \text{ μs}$ )

## REFERENCES

1. Gold, V. M.; Vradis, G. C.; and Pearson, J. C., "Penetration of Concrete by Eroding Projectiles: Experiments and Analysis," ASCE J. Eng. Mech., Vol. 122, No. 2, pp 145-152, 1996.
2. Tate, A., "A Theory for Deceleration of Long Rods After Impact," J. Mech. Phys. Solids, Vol. 15, pp 387-399, 1967.
3. Tate, A., "Further Results in the Theory of Long Rod Penetration," J. Mech. Phys. Solids, Vol. 17, pp141-150, 1969.
4. Tate, A., 1986??
5. Pidsley, P. H., "A Numerical Study of Long Rod Impact onto a Large Target," Int. J. Mech. Sci., Vol. 32, pp 315-333, 1984.
6. Anderson, C. E. and Walker, J. D., "Long-Rod Penetration and the Calculation of Target Resistance," Shock Compression of Condensed Matter, S. C. Schmidt, R. D. Dick, J. W. Forbes, D. G. Tasker (editors), pp 967-970, Elsevier Science Publishers, 1991.
7. Anderson, C. E. and Walker J. D., "An Examination of Long-Rod Penetration," Int. J. Impact Engng, Vol. 11, pp 481-501, 1991b.
8. Gold, V. M.; Vradis, G. C.; and Pearson, J. C., "A Study of Constitutive Models for Concrete Penetration Analysis," ASCE J. Eng. Mech., Vol. 122, No. 3, pp 230-238, 1996.
9. Tipton, R. E., "CALE Users Manual," Version 910201, Lawrence Livermore National Laboratory, Livermore, California, 1991.
10. Wilkins, M. L., "Calculations of Elastic-Plastic Flow," Methods of Computational Physics, Adler B., Fernbach S., Rotenberg M. (eds), Vol. 3, pp 211-263, New York, Academic Press, 1964.
11. Wilkins, M. L., "Calculations of Elastic-Plastic Flow," UCRL-7322, Rev. 1, Lawrence Livermore National Laboratory, 1969.
12. Steinberg, D. J.; Cochran, S. G.; and Guinan, M. W., "A Constitutive Model for Metals Applicable at High-strain Rate," J. Appl. Phys., Vol. 51, No. 3, pp 1498-1504, 1980.
13. Tipton R. E., "EOS Coefficients for the CALE Code for Some Materials," Lawrence Livermore National Laboratory, Livermore, California, 1991.

14. Read, H. E. and Maiden, C. J., "The Dynamic Behavior of Concrete," S-CUBED Report 3SR-707, Systems, Science and Software Corporation, La Jolla, California, 1971.
15. Tipton, R. E., "Porous EOS in CALE Used to Model Concrete," Lawrence Livermore National Laboratory, Livermore, California, 1991.
16. Smith, J., Private Communications, Lawrence Livermore National Laboratory, Livermore, California, 1993.
17. Christman, D. R. and Gehring, J. W., "Analysis of High-Velocity Penetration Mechanics," J. Appl. Phys., Vol. 37, pp 1579-1587, 1966.
18. Gehring, J. W., Jr., "Theory of Impact on Thin Targets and Shields and Correlation with Experiment," High Velocity Impact Phenomena, R. Kinslow (ed.), pp 105-156, Academic Press, New York and London, 1970.
19. Alekseevskii, V. P., "Penetration of a Rod into a Target at High Velocity," Combustion, Explosion and Shock Waves, Vol. 2, pp 63-66 (translated from the Russian), Faraday Press, New York, 1966.
20. Pei-Rong, Lin and Batra, R. C., "Histories of the Stress, Strain-Rate, Temperature and Spin in Steady State Penetration Problems," Int. J. Engng Sci., Vol. 27, pp 1155-1165, 1989.
21. Walker, J. D. and Anderson, C. E., Jr., "The Influence of the Initial Nose Shape on the Shock Phase of the Impact," Shock Compression of Condensed Matter - 1991, S. C. Schmidt, R. D. Dick, J. W. Forbes, D. G. Tasker (eds), pp 943-946, Elsevier Science Publishers, 1992.
22. Walker, J. D. and Anderson, C. E., Jr., "The Influence of the Initial Nose Shape in Eroding Penetration," Int. J. Impact Engng, Vol. 15, pp 139-148, 1994.
23. Walker, J. D. and Anderson, C. E., Jr., "A Time-Dependent Model for Long-Rod Penetration," Int. J. Impact Engng, Vol. 16, pp 19-48, 1995.
24. Birkhoff, G.; MacDougall, D. P.; Pugh, E. M. and Sir Taylor, G., "Explosives with Lined Cavities," J. Appl. Phys., Vol. 19, pp 563-582, 1948.
25. Eichelberger R. J., "Experimental Test of the Theory of Penetration by Metallic Jets," J. Appl. Phys., Vol. 27, pp 63-68, 1956.
26. Bishop, R. F.; Hill, R.; and Mott, N. F. "The theory of Indentation and Hardness Tests," Proc. Phys. Soc., Vol. 57(3), pp 147-159, 1945.



## DISTRIBUTION LIST

Commander

Armament Research, Development and Engineering Center

U.S. Army Tank-automotive and Armaments Command

ATTN: AMSTA-AR-LSL (2)

AMSTA-AR-GCL

AMSTA-AR-WEE

AMSTA-AR-WEE-C (5)

Picatinny Arsenal, NJ 07806-5000

Defense Technical Information Center (DTIC)

ATTN: Accession Division

8725 John J. Kingman Road, Suite 0944

Fort Belvoir, VA 22060-6218

Director

U.S. Army Materiel Systems Analysis Activity

ATTN: AMXSY-EI

392 Hopkins Road

Aberdeen Proving Ground, MD 21010-5423

Commander

Chemical/Biological Defense Agency

U.S. Army Armament, Munitions and Chemical Command

ATTN: AMSCB-CII, Library

Aberdeen Proving Ground, MD 21010-5423

Director

U.S. Army Edgewood Research, Development and Engineering Center

ATTN: SCBRD-RTB (Aerodynamics Technology Team)

Aberdeen Proving Ground, MD 21010-5423

Director

U.S. Army Research Laboratory

ATTN: AMSRL-OP-CI-B, Technical Library

Aberdeen Proving Ground, MD 21005-5066

Chief

Benet Weapons Laboratory, CCAC

Armament Research, Development and Engineering Center

U.S. Army Tank-automotive and Armaments Command

ATTN: AMSTA-AR-CCB-TL

Watervliet, NY 12189-5000

Director  
U.S. Army TRADOC Analysis Command - WSMR  
ATTN: ATRC-WSS-R  
White Sands Missile Range, NM 88002

Commander  
Naval Air Warfare Center Weapons Division  
1 Administration Circle  
ATTN: Code 473C1D, Carolyn Dettling (2)  
China Lake, CA 93555-6001

GIDEP Operations Center  
P.O. Box 8000  
Corona, VA 91718-8000

U.S. Air Force Materiel Command  
Aeronautical Systems Center  
ATTN: YOC, CPT D. Nichols  
314 W. Choctawhatchee Ave, Suite 104  
Eglin AFB, FL 32542-5000

U.S. Air Force Material Command  
Aeronautical Systems Center  
ATTN: ASC/YV, L. Davila  
102 West D Ave, Suite 168  
Eglin AFB, FL 32542-7210

U.S. Air Force Space Warfare Center  
ATTN: SWC/AE, J. Andros  
720 Irwin Ave, Suite 203-4  
Falcon AFB, CO 80912-7210

Air Force Institute of Technology  
Air University  
ATTN: Technical Library  
Wright-Patterson AFB, OH 45433

Air Force Office of Scientific Research  
ATTN: Technical Library  
Bolling AFB, DC 20332

Phillips Laboratory  
ATTN: Technical Library  
Kirtland AFB, NM 87117-6008

Wright Laboratory  
Airbase Survivability Branch  
ATTN: WL/FIVCO, W. S. Strickland  
139 Barnes Drive, Suite 2  
Tyndall AFB, FL 32403-5323

Commander  
Wright Laboratory  
Armament Directorate  
ATTN: MNMW, Y. Tu  
          W. Cook  
          MNMF, D. Mabry  
          MNSA, K. Milligan, Suite 326  
          B. Patterson, Suite 326  
          J. Foster  
          L. Lijeucsky  
101 W. Eglin Blvd  
Eglin AFB, FL 32542-6810

Lawrence Livermore National Laboratory  
ATTN: L-53, Technical Library  
P.O. Box 808  
Livermore, CA 94550-0622

Los Alamos National Laboratory  
ATTN: M/S F607, M. Schick  
          M/S P364, Report Library  
P.O. Box 1663  
Los Alamos, NM 87545

Sandia National Laboratories  
ATTN: Dept 9823, M. Forrestal, M/S 0312  
          J. Hickerson, M/S 0303  
          Dept 2411, D. Davidson, M/S 0303  
          Detp 7141, Technical Library, M/S 0889  
P.O. Box 5800  
Albuquerque, NM 87185

Sandia National Laboratories  
ATTN: Division 8316, J. Lipkin  
          Technical Library, M/S 9211  
Livermore, CA 94550